THESIS FOR THE DEGREE OF LICENTIATE OF ENGINEERING

Design and Evaluation of a Permanent Magnet Generator for Wave Power Applications

PINAR TOKAT

Department of Energy and Environment
CHALMERS UNIVERSITY OF TECHNOLOGY
Göteborg, Sweden 2015

Design and Evaluation of a Permanent Magnet Generator for Wave Power Applications

PINAR TOKAT

Department of Energy and Environment
CHALMERS UNIVERSITY OF TECHNOLOGY
SE-412 96 Göteborg
Sweden
Telephone + 46 (0)31 772 16 63

To my family...

Abstract

In this thesis, the performance of a wave energy converter (WEC) consisting of a single point absorber wave device coupled with a radial flux permanent magnet generator is investigated. The available wave power and the energy potential are studied for a specified wave climate and the electric power output is determined through a buoy movement simulation. Based on the ideal buoy size determined for the selected wave climate and the resulting generator power, different rotor designs of a suitable permanent magnet machine are investigated.

By implementing different generator designs into the WEC, the efficiency maps of the WEC generators are investigated. Furthermore, for a better understanding of the economical feasibility of the system, life cycle cost (LCC) analysis is performed on the different generator designs. The inset design is further improved by replacing the initial materials with better performance materials. Despite the cost increase due to using higher performance materials, an important finding was that the capitalised losses account for the majority of the LCC. Therefore, the improved magnet and iron materials are well motivated, since such a design results in a lower LCC.

Acknowledgement

The research was carried out in collaboration with the Ocean Energy Centre and financed by Västra Götalandsregionen and Areas of Advance in Energy at Chalmers University of Technology. The financial support is gratefully appreciated.

I would like to sincerely thank my supervisor Torbjörn Thiringer, my examiner Ola Carlson and my co-supervisor Johan Åström for their guidance and support throughout the project. I would especially like to thank Torbjörn not only for his tremendous patience and support during the project but also for the fun conversations off work. Additionally, I would also like to take this opportunity to thank Lars Bergdahl and Johannes Palm from the Department of Shipping and Marine Technology for their help.

A big thank you to all my colleagues at the division of Electric Power Engineering , for making it possible for me to have a very friendly and comfortable work place. A special thank you goes to my office mates, Joachim Härsjö, Pavan Balram, Nicolas Espinoza, Daniel Pehrman and Pramod Bangalore for always listening to me and keeping the humor level high in the office.

Finally, I would like to direct my gratitude to my family and my friends, for the unconditional love and support, which forever motivates me to be worthy of.

Contents

List of Nomenclatures

WEC	Wave Energy Converter
PM	Permanent Magnet
MTPA	Maximum Torque per Ampere
NPVL	Net Present Value of Losses
LCC	Life Cycle Cost
θ_{ex}	Phase shift of the wave excitation
ϑ_p	particle velocity
λ	Wave length
μ	Permeability
$\Pi_{material}$	Material price
ρ	Water density
ρ_{cu}	Copper resistivity
Φ	Flux
ϕ	Power angle
φ	MTPA Angle
Ψ	Flux linkage
Ψ_m	Magnet flux linkage
ω	Angular frequency of the wave
ω_r	Electrical speed
A	Added mass coefficient
a	Wave amplitude
B	Radiation damping coefficient
B	Flux density
C	Hydrostatic stiffness
C_d	Drag coefficient
$C_{investment}$	Investment cost
c_{ex}	excitation coefficient
E_{off}	Turn off losses
E_{on}	Turn on losses
E_{sw}	Total switching losses
F_b	Buoyancy force

F_d	Drag force
F_{exc}	Wave excitation force
F_{hyd}	Hydrostatic force
F_p	Power extraction force
F_r	Radiation force
f_{sw}	Switching frequency
g	Gravitational acceleration
H	Wave height
H	Field intensity
H_{sub}	Height of the submerged part
i	Interest rate
i_i	Current of i
J	Current density
k	Wave number
k_i	Exponent of current dependency for switching loss calculation
k_v	Exponent of current dependency for switching loss calculation
L_{sd}	d-axis stator inductance
L_{sq}	q-axis stator inductance
l_a	stack length
l_{ew}	end winding length
M	Modulation index
$m_{material}$	Material weight
N	Number of turns
N_{pb}	Number of parallel branches
n	Mechanical speed in rpm
n_p	Number of pole pairs
p	Probability
R_p	Power extraction coefficient
R_s	Stator resistance
R_T	Internal resistance
R_t	Net cash flow
r_b	Buoy radius
T	Wave period
V_i	Voltage of i
V_T	Threshold voltage
x	horizontal position
z	Vertical position

Chapter 1

Introduction

1.1 Background

The demand for electricity has been increasing with the increasing population, the higher life standards and the technological developments. In order to supply the increasing energy demand, yet not contribute more to greenhouse gas emissions, the popularity of the sustainable energy sources for electricity generation has been increasing. The European Union's 2020 climate and energy package aims to reduce the greenhouse gas emissions by 20% while raising the energy produced by the sustainable resources to 20% of the total energy consumption in Europe.

Solar and wind power are popular sustainable energy sources and are widely available for electricity production. Since the wind is generated by the solar heating, wave energy can be considered as a concentrated form of solar energy. An order of 100 W/m^2 solar radiation can be transferred into ocean waves which have the potential of up to 1000 kW/m of wave crest length. Estimates of the worldwide economically recoverable wave energy resource are 140 to 750 TWh/year, for existing wave energy converter (WEC) technologies [1].

Compared with the mentioned forms of renewable energy, the power fluctuations for the ocean waves are small over a long period of time. This categorizes wave energy as a viable renewable energy resource and economically comparable to the more traditional renewable energy resources [2]. Despite the positive reasons above, wave power plants are still not widely spread. The main challenges associated with electricity production through ocean waves are the mechanical system development to be able to harness the wave energy efficiently as well as the harsh ocean environment and its requirements on the system components, which lead to high system costs. Another impor-

tant challenge regarding the wave power production is the fluctuating power levels. The available wave power can differ immensely from a calm sea state to a highly excited sea state [3]. This brings up a challenge for designing the WEC, which can withstand the high power levels, yet efficiently operate for the calmer sea states. There are a handful of wave power stations currently operational and the average capacity of these plants are approximately 400 kW [4].

1.2 Previous Work and Challenges

Much effort has been directed towards studying the electricity production using ocean waves. One of the most popular wave energy devices are based on a point absorber technology. For example, [5] present studies of effective power take-off strategies for a point absorber type WEC.

There are a number of studies regarding topologies coupling the point absorber to a linear generator for electricity generation. The leading research on linear generators used for wave energy applications is the Uppsala Project and [6] shows an overview of the project. For further information [7–10] can be useful. Another interesting study is held for a tubular linear generator system designed for the Italian coast, an overview can be seen in [11]. The rotating generators are not commonly studied for wave energy applications, yet there are a few investigations using an induction machine. The induction machine utilized can be a conventional induction generator with stator connected power electronic control [12] or a doubly-fed induction generator, which is widely available for wind power applications currently [13]. There are a few researches done using rotating permanent magnet (PM) generators for wave power applications [14], however studies regarding the design and efficiency of a rotating permanent magnet generators for a point absorber system has not been found in available literature.

Regarding the energy optimization using rotor geometry alterations, [15] shows an extensive study on V-shaped magnet PM machine optimization through design studies for operation with a wide constant power speed region. The air gap flux density has a great impact on the generated torque of the PM machine and one of the most efficient ways to tune the air gap flux density waveform in a rotating PM machine is to optimally set the magnet shape, orientation, when the volume and the air gap distance is kept the same [16]. In [17], different permanent magnet arrangements are studied in order to reduce the amount of magnet material used for a permanent magnet traction motor. Design aspects of the magnet placement are also studied in [18], in this case for permanent magnet assisted synchronous reluctance

machines.

Regarding the permanent magnet machine type selection for a wind power plant, [19] has valuable results, showing that the surface mounted PM generator has lower efficiency due to a lower power factor, compared to an interior mounted design, using the same magnet volume.

1.3 Purpose of Work

The purpose of the work is to design and optimize a high efficiency permanent magnet generator suitable for wave power production.

In order to achieve this goal, first an initial permanent magnet generator is to be designed for the required power level. From then on, this generator is to be optimized with regards to efficiency, by the means of rotor geometry alterations and material modifications.

However, only establishing the energy efficiency levels of the different designs does not provide a concrete answer of which one that is the most suitable design for a WEC. Therefore, economical evaluations are performed in order to obtain the life cycle cost of each investigated design.

Chapter 2

Wave Theory

2.1 Single frequency regular wave motion

Ocean waves are produced by the wind and are of stochastic nature. These waves are irregular and can be represented as a superposition of different frequencies. The sole information about the irregular waves are the amplitude and period of each harmonic wave, as well as their direction of propagation [20]. One possible representation, which is used in this work is to consider them as a set of regular waves, each being a single frequency sine wave. This method is very common regarding energy capture studies, as can be seen in [21–23]. The sinusoidal formed ocean waves are defined using a couple of parameters. One of these parameters is the wave period, T, which is the time taken for one full oscillation of the wave. Another important parameter is the wave height, H, and is defined as the vertical distance from crest to trough, whereas the wave amplitude, a, is the height between the mean water surface to the wave crest. Figure 2.1 shows the base wave representation with respect of time.

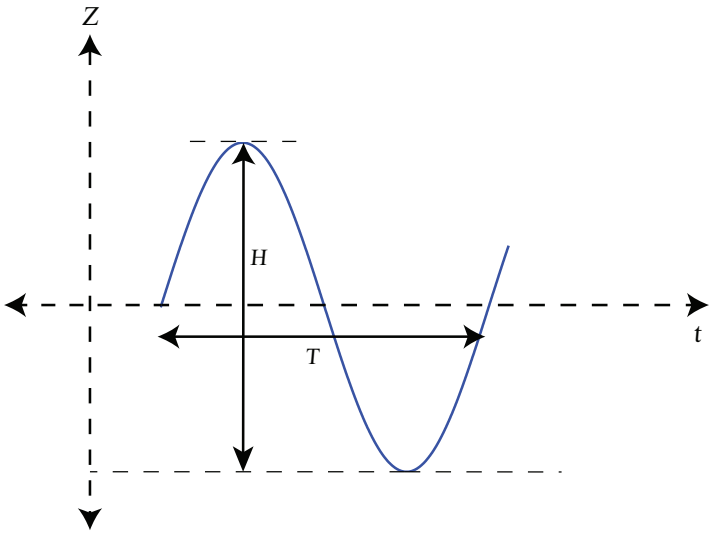

Figure 2.1: General regular wave representation in time domain, for a fixed position.

Furthermore, the wave length, λ, is the horizontal distance between two following wave crests. Figure 2.2 shows the wave representation where the horizontal axis denotes the x-axis. Here, t denotes the time and x is the position on the x-axis.

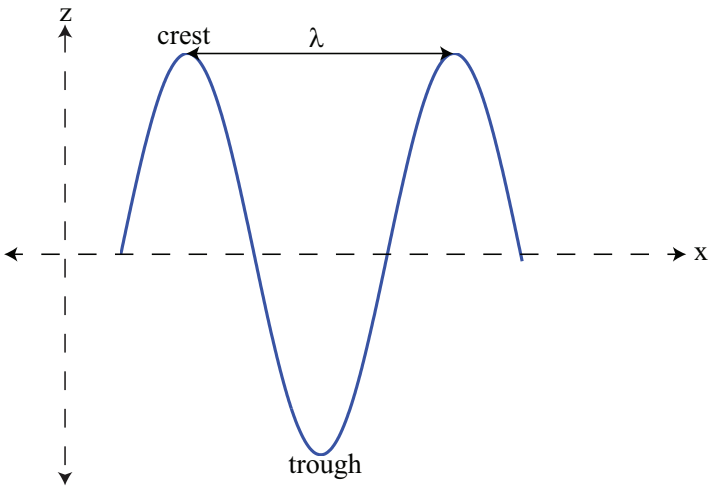

Figure 2.2: General regular wave representation on the water surface, at a fixed time instant.

The point where the wave has the maximum upward displacement within a cycle is called a wave crest and the opposite is the wave trough. Since the wave period is known, the wave frequency can be calculated. The angular frequency of the wave is

$$\omega = \frac{2\pi}{T} \tag{2.1}$$

The number of radians per unit distance, also known as the wave number, k, is then

$$k = \frac{2\pi}{\lambda} \tag{2.2}$$

And finally the wave elevation for a single frequency regular wave then becomes,

$$z_w(t, x) = a\cos(\omega t - kx) \tag{2.3}$$

where z_w is the wave elevation, ω is the angular frequency of the wave.

2.2 Equation of motion

In this section, the interaction between the floating object and the water will be described, in order to be able to simulate the motion of a floating body located in the ocean. Placing the floating object in the water would clearly have some consequences, considering that the object is to be placed at the surface where the wave energy propagates the most. The interaction of the object and the waves will cause disturbance to the natural motion of the waves and due to this, there will be some forces acting on the buoy. These forces acting on the buoy result in six modes of motions in a 3 dimensional space. Figure 2.3 shows the direction of the six different motions of the buoy.

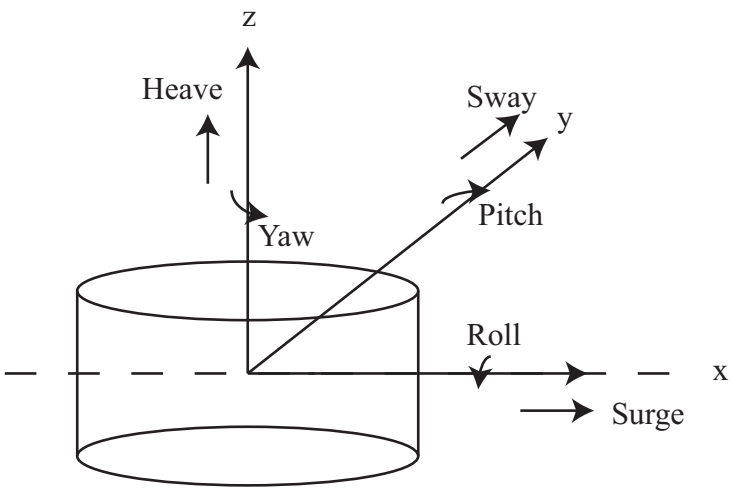

Figure 2.3: Six modes of motions on a rigid floating object.

As it is observed from Figure 2.3, there is a linear and a rotating motion on each axes of the coordinate system. The linear motions are called, surge, sway and heave in x,y,z directions, respectively [20]. Similarly rotating motions are named as roll, pitch and yaw in the same order. The motion of the floating object is to be calculated for six degrees of freedom.

Figure 2.4 shows the mechanical representation of one single degree of freedom floating object system.

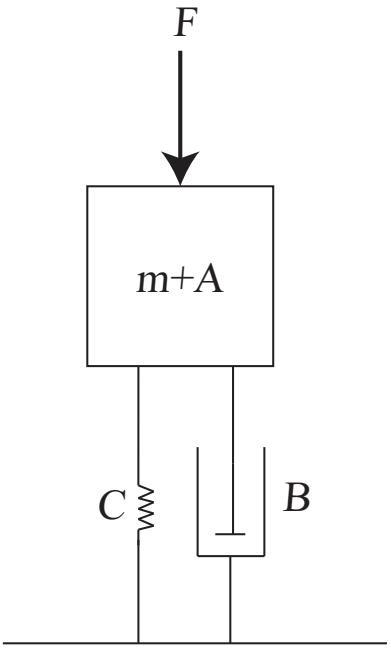

Figure 2.4: Mechanical representation of a floating object for heave motion.

Here, A is added mass, B is the radiation damping, C is the hydrostatic stiffness, m is the buoy mass and F is the force [24]. The motion of the floating body can be expressed as,

$$\overrightarrow{M} \cdot \ddot{\overrightarrow{z_b}} = \overrightarrow{F} \tag{2.4}$$

where M is the mass matrix of the floating body, $\ddot{z}_b$ is the buoy acceleration and F is the total force vector acting on the body. All the parameters are in vector format and they are represented for all six modes of motion. The forces acting on the body can be divided into individual forces according to their origin. Thus, F can be rewritten as,

$$\overrightarrow{F} = \overrightarrow{F}_e + \overrightarrow{F}_{hr} + \overrightarrow{F}_p \tag{2.5}$$

Here, $\overrightarrow{F}_e$ represents the wave excited forces while the floating body stands still, $\overrightarrow{F}_{hr}$ represents the hydrodynamic reaction forces created while the body is oscillating in still water. These forces are determined as the buoy is oscillating. In case a generator is connected to the floating object, its power extraction is represented by $\overrightarrow{F}_p$. The hydrodynamic reaction force consists of several components according to their hydrodynamic properties defined using three variables. In this thesis, only heave motion is considered and the

equations below are formulated for one single degree of freedom, movement in the z-direction. The positive reference is selected as the upward z-direction.

$$F_{hr} = -A \cdot \ddot{z}_b - B \cdot \dot{z}_b - C \cdot z_b \tag{2.6}$$

Combining (2.5) and (2.6), the equation of motion of a floating body in the ocean can be expressed as

$$(M + A) \cdot \ddot{z}_b = F_e - B \cdot \dot{z}_b - C \cdot z_b + F_p \tag{2.7}$$

where,

$$F_r = B \cdot \dot{z}_b \tag{2.8}$$

and

$$F_{hyd} = C \cdot z_b \tag{2.9}$$

Here, F_r represents the radiation force and F_{hyd} represents the hydrostatic force. Knowing these, (2.7) can be rewritten as;

$$(M + A) \cdot \ddot{z}_b = F_e - F_r - F_{hyd} + F_p \tag{2.10}$$

Here, F_e is the wave excited force in z-direction, which is to be referred as the wave excitation force and is defined as

$$F_{exc} = c_{exc} \frac{H}{2} \cos(\omega t - \theta_{exc}) \tag{2.11}$$

where c_{exc} is the excitation coefficient and θ_{exc} is the phase shift of the wave excitation from the wave. It is important to express that for the bodies floating at the water surface, added mass,radiation damping and wave excitation coefficients are frequency dependent [24].

2.2.1 Added Mass

Added mass is the inertia added to the floating object while it oscillates at the sea surface and it originates due to the fact that when the body moves, the water surrounding it moves as well. Added mass is a frequency dependent parameter for the objects that float on/near the surface, yet it becomes less and less frequency dependent when the object gets closer to the sea bottom. Similarly, when the oscillation frequency is very high, the added mass coefficient becomes a constant.

2.2.2 Radiation Damping

As mentioned before, oscillation of the floating body causes displacement of the surrounding fluid. The motion of the floating body causes waves which radiate out of the system. The force that sustains the oscillating motion will then be in phase with the velocity. Since the radiated waves would transport energy away from the body, this motion creates a hydrodynamic damping. For the bodies that stand still or oscillate with infinite frequency, the radiation damping is zero.

2.2.3 Wave Excitation

A floating object is effected by incoming waves. In order to calculate the wave excitation force, the wave excitation coefficient must be known. This coefficient, similar to radiation damping and added mass, is frequency dependent and is represented with an amplitude as well as an angle. The reason for the wave excitation angle is that there is a phase shift between the buoy movement and the wave elevation. In this work, added mass, radiation damping and the wave excitation coefficient are determined through [25].

2.3 Available Wave Power

The ocean waves contain energy and the amount of this energy depends on the property of the wave. The available energy per meter wave crest during a certain time duration is

$$E_{wave} = \int_0^t P_{wave} dt \tag{2.12}$$

The available wave power for a regular wave, P_{wave}, is the transport of the energy through the ocean by waves and is denoted as

$$P_{wave} = \frac{1}{32\pi} \rho g^2 H^2 T \tag{2.13}$$

where ρ is the density of the sea water. The wave power is captured by a unit, which will be called "wave energy converter (WEC)", where the electricity generation will take place. For irregular waves, the available wave power can be determined using

$$P_{wave} = \frac{1}{64\pi} \rho g^2 H_s^2 T_z \tag{2.14}$$

where H_s is the significant wave height and T_z is mean zero crossing period. H_s is the average height of the highest 1/3 of the waves and T_z is the average of the zero crossing periods of the irregular waves. The wave heights and the wave periods are determined from the sea measurements performed for a specific duration. The combination of these parameters are sorted with respect to their occurrence. The long term statistical representation of sea states is called a scatter diagram and it depicts the probability of occurrence of H_s and T_z [24].

2.4 Single Point Absorber Model

The electric generator is driven by the force which is created by the movement of the buoy. In this project, the point absorber is a cylindrical buoy and the water depth is selected to be 50 m. Figure 2.5 shows the representation of the buoy.

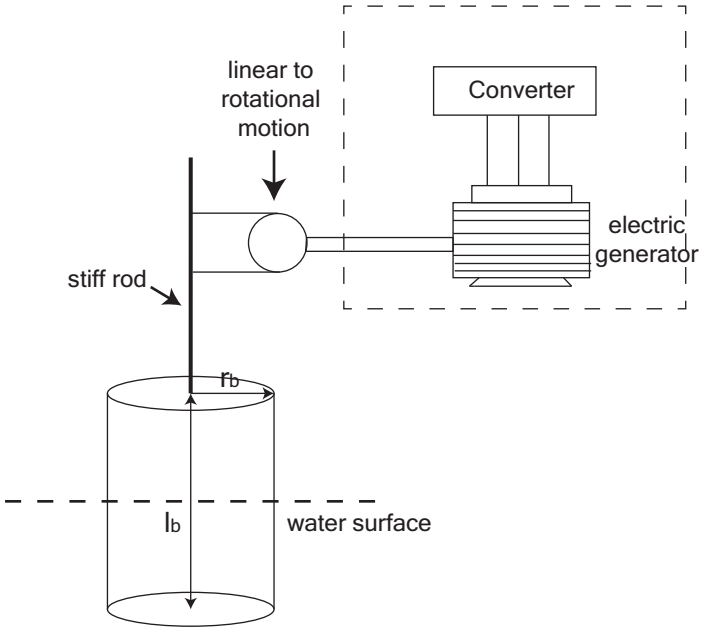

Figure 2.5: Representation of the single point absorber model.

The length and the radius of the buoy will be selected to fit the operation environment. The radiation and the hydrostatic forces are calculated according to (2.8) and (2.9). The hydrostatic stiffness constant in (2.9) can be determined as

$$C = \rho g A_{buoy} \tag{2.15}$$

where ρ is the water density, g is the gravitational acceleration and A_{buoy} is the area of the buoy.

The power extraction in this work is assumed to be passive and the electric generator is considered to be a function of the buoy position. The power extraction force set up by the generator and made to be proportional to the speed. It is calculated as

$$F_p = -R_p \dot{z_w} \tag{2.16}$$

where R_p is the power extraction coefficient and is optimized for each $H - T$ combination through an optimization procedure.

The next force acting on the buoy is the drag force, F_d. Drag is the resistance of the water that acts on the buoy and it is in the direction of the relative fluid flow velocity for the buoy. Therefore, to be able to determine the drag force that acts on the buoy, the relative velocity is to be obtained first.

The vertical position of the wave is given by (2.3). The vertical wave velocity is the time derivative of the wave position and given as

$$\dot{z_w} = -\frac{H}{T}\pi \sin(\omega t) \tag{2.17}$$

where $\dot{z_w}$ represents the wave velocity. To be able to determine the relative velocity, the particle velocity of the water should also be known [24]. The particle velocity is

$$\vartheta_p = \dot{z_w} e^{-kH_{sub}} \tag{2.18}$$

Here H_{sub} is the height of a part of the buoy which is considered to be submerged as default. The relative velocity is then calculated by subtracting the wave velocity from the particle velocity. The drag force then can be calculated as

$$F_d = \frac{1}{2}\rho\pi C_d r_b^2 [(\vartheta_p - \dot{z_b})|(\vartheta_p - \dot{z_b})|] \tag{2.19}$$

Here, C_d is the drag coefficient and it mainly depends on the geometry of the object. It can be observed that the drag force is a function of the velocity squared.

According to the above, the total force acting on the buoy is

$$F = F_{hyd} + F_{exc} + F_r + F_p + F_d \tag{2.20}$$

Chapter 3

The Electrical Drive System

This chapter explains the electromagnetic background necessary to explain the operation principles of a permanent magnet machine. Figure 3.1 shows a basic electromagnetic circuit which illustrates how a magnetic flux through an iron path and an air gap is created.

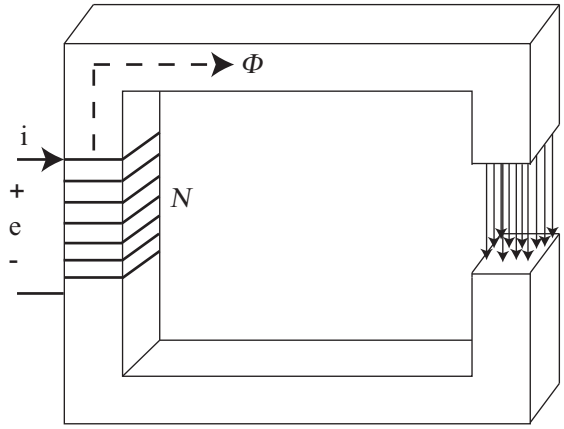

Figure 3.1: Basic magnetic circuit illustrating how a magnetic flux is created by a current.

Here, a conductor is wrapped on an iron core with an air gap. When a current is applied to the conductor, a magnetic field will be generated. The resulting flux of this magnetic field will travel through the iron core and through the air gap. If the fringing effects [26] are ignored, the flux will be the same throughout the iron core and the air gap. The enclosed current for a coil is

$$I_{enclosed} = NI \tag{3.1}$$

where N is the number of turns of the conductor that creates the coil. The flux can be represented as

$$\Phi = \int\int BdS \tag{3.2}$$

where B is the flux density and dS is the differential area. For the simple geometry shown above, flux can be reformulated as

$$\Phi = BA_{core} \tag{3.3}$$

Here, the unit of the flux is Weber and the flux density unit is Tesla (Wb/m^2). A_{core} is the core area. The direction of the flux can be determined by the "Right Hand Rule" , with the knowledge of the current direction.

Ampere's Law dictates the relation between the magnetic field and the enclosed current and is represented as

$$\oint Hdl = \int\int JdS = I_{enclosed} \tag{3.4}$$

where H is the field intensity in A/m, dl is the differential length in meters. J is the current density. Here, the magnetic flux density is related to the magnetic fiend intensity as

$$B = \mu H \tag{3.5}$$

μ is the permeability of the material and defined as

$$\mu = \mu_0 \mu_r \tag{3.6}$$

where μ_0 is the permeability of free space and μ_r is the relative permeability. Relative permeability for air air is approximately 1, whereas the iron material has a very high permeability, up to 10000. Due to this fact, the field intensity is much higher in the air gap, than it is in the iron core. Relative permeability varies strongly with the flux density and for very high flux levels it will go towards 1. For the structure shown in Figure 3.1, the flux density is the same for the whole object. However, in an electric machine which has a complicated iron geometry, the flux density will differ with regards to the geometry, as well as the relative permeability of the material. Observe that the relative permeability is a function of the flux. This makes analytical calculations for electric machine quite complicated. Therefore, typically for machine analysis Finite Element Method (FEM) calculations are used.

An important quantity is the he total flux linkage and it is related to the flux according to

$$\Psi = N\Phi_c \tag{3.7}$$

Φ_c is the flux in the coil and Ψ represents the total flux linkage. The flux linkage is related to the induced voltage in the coil as

$$e = -\frac{d\Psi}{dt} \tag{3.8}$$

where e is the electromotive force (emf). This means that the induced emf in a closed circuit is equal to the negative value of the time derivative of the enclosed magnetic flux and is called Faraday's Law of Induction.

The inductance of the electromagnetic circuit is formulated as

$$L = \frac{\Psi}{I} \tag{3.9}$$

The winding can be represented as a resistance and an inductance, which causes a voltage drop over it. The current-voltage relation can be calculated as

$$v = L\frac{di}{dt} + Ri \tag{3.10}$$

where R is the resistance of the wire.

Figure 3.2 shows the same electromagnetic circuit shown above, with a magnet placed in the air gap, which rotates with the angular speed of ω_r.

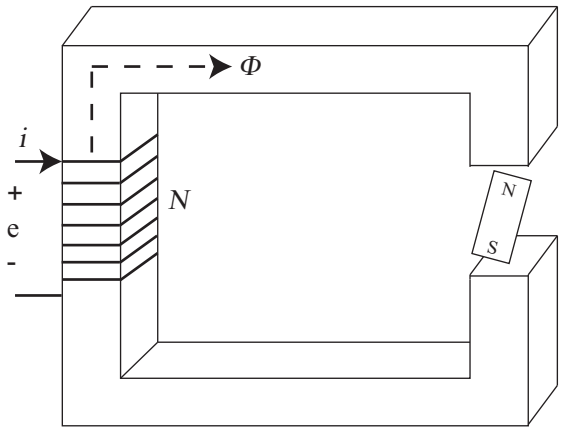

Figure 3.2: Basic magnetic circuit illustrating .

This is the most basic principle of the electric machine operation. The current-voltage relation now becomes

$$v = L\frac{di}{dt} + Ri + \omega_r \Psi_m \cos(\omega_r t) \tag{3.11}$$

where Ψ_m is the flux linkage of the magnet and ω_r is the speed of the magnet rotation.

The expressions above show the electromagnetic relations for a basic circuit. These expressions can be applied to the electric machines.

Figure 3.3 shows a reduced representation of a permanent magnet generator.

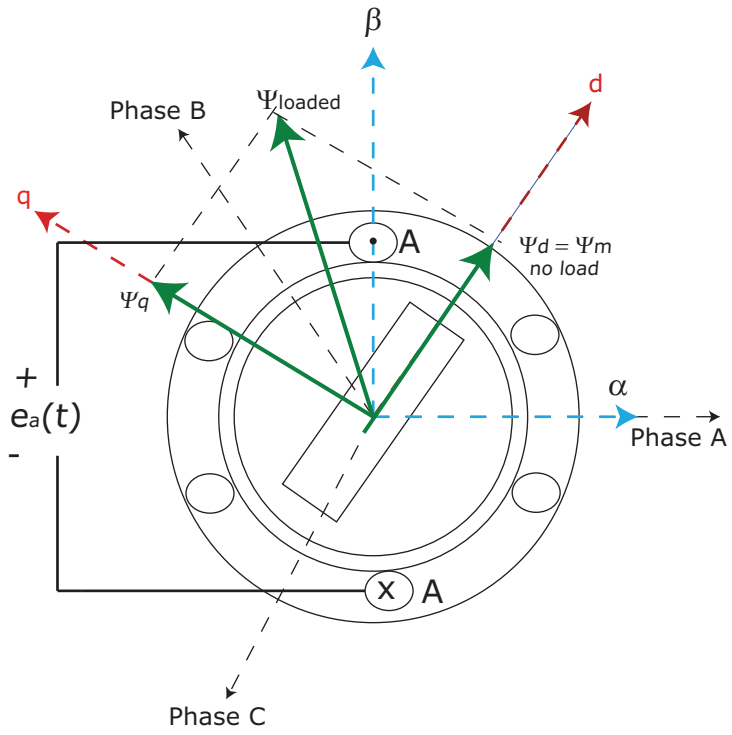

Figure 3.3: Simplified electromagnetic representation of a permanent magnet machine, displaying direct and quadrature directions.

Phase A, Phase B and Phase C lines show the magnetic axes for each stator current phase and they are oriented 120^o apart from each other. The winding of Phase A is schematically displayed in the figure, where the magnetic direction is dictated through the right hand rule. It is important to know that the A-coil typically has several turns and might also be distributed in more than one slot. The induced voltage outlet for the A phase, where (3.8) is applicable when the resistance is ignored, is depicted in the figure.

In order to simplify the three phase analysis of the generator, d-q transformation can be used. d-q transformation is a method which reduces the three AC quantities regarding each phase into two DC quantities. The flux

linkage in the machine is represented in the d-q axis where the d-axis represents the direction of the magnet flux [27]. For no load operation, the d-axis flux linkage is the same as the magnet flux linkage, which also is the total flux linkage of the generator. However, for the loaded case, a flux linkage on the q-axis will be formed, which then contributes to a resulting total flux linkage together with the magnet flux linkage as well as the d-axis flux linkage component created by the d-axis current.

3.1 Permanent Magnet Machine

The permanent magnet (PM) machine rotor consists of permanent magnets for creating the rotor excitation. In a PM machine, the rotor losses are greatly lowered compared to those in an induction machine, due to not having windings in the rotor. There are several types of permanent magnet machines, using different magnet placements and are called, Surface Mounted, Inset Mounted or Interior Mounted PM. Figure 3.4 shows some of the different PM type designs [28].

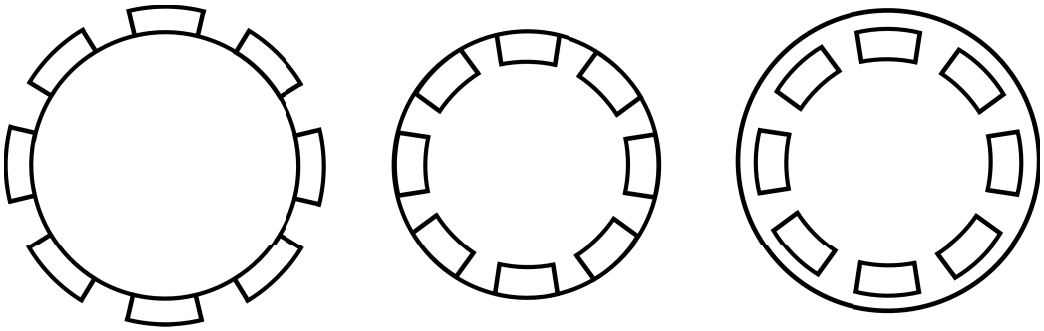

Figure 3.4: PM machine variants. Surface mounted, Inset mounted, Interior mounted respectively.

The PM machine used in this work, which is also the most common variant for the kW level power applications, is a 3-phase machine operated with sinusoidal input current. The stator equations for the PM machine in d-q directions are

$$u_{sd} = R_s i_{sd} + L_{sd}\frac{di_{sd}}{dt} - \omega_r L_{sq} i_{sq} \tag{3.12}$$

$$u_{sq} = R_s i_{sq} + L_{sq}\frac{di_{sq}}{dt} + \omega_r L_{sd} i_{sd} + \omega_r \Psi_m \tag{3.13}$$

Here R_s is the stator resistance, L_{sd} and L_{sq} are the stator inductances in d and q coordinates respectively. ω_r is the electrical rotor angular speed and Ψ_m is the flux linkage caused only by the magnet. The initial value of Ψ_m can be determined by the no load test but it is dependent on the q-axis current and it is determined for various q-axis currents when the d-axis current is zero. Therefore, while performing the machine analysis it is represented as a function of the q-axis current. For a broader description, [29] can be studied. The magnet flux linkage reduces for increasing q-axis current due to saturation. The d and q axis inductances also vary, due to the same reason [29]. The current derivatives in (3.12) and (3.13) indicate electrical dynamics. However, since the mechanical system has a much lower time constant than the electrical one, the electrical behaviour is considered in steady state. The stator equations then become

$$u_{sd} = R_s i_{sd} - \omega_r L_{sq} i_{sq} \tag{3.14}$$

$$u_{sq} = R_s i_{sq} + \omega_r L_{sd} i_{sd} + \omega_r \Psi_m \tag{3.15}$$

where the current derivative term is neglected. Using analytical calculations for simplified cases or as in this work FEM calculations, the flux linkages in d and q directions can be determined for various operating points. From these, the stator inductances in d-q axis can be calculated as

$$L_{sd} = \frac{\Psi_d - \Psi_m}{i_{sd}} \tag{3.16}$$

$$L_{sq} = \frac{\Psi_q}{i_{sq}} \tag{3.17}$$

where Ψ_d and Ψ_q are the flux linkages in d and q directions respectively.

The electromagnetic torque of the permanent magnet machine is modelled as [27]

$$T_e = \frac{3n_p}{2}(\Psi_m i_{sq} + (L_{sd} - L_{sq}) i_{sd} i_{sq}) \tag{3.18}$$

where n_p is the number of pole pairs. The torque equation can be split in two parts as

$$T_e = T_M + T_R \tag{3.19}$$

where T_M is the magnet torque and is

$$T_M = \frac{3n_p}{2}(\Psi_m i_{sq}) \tag{3.20}$$

and T_R is the reluctance torque and is

$$T_R = \frac{3n_p}{2}(L_{sd} - L_{sq})i_{sd}i_{sq} \tag{3.21}$$

3.2 Converter

For the machine control, a three phase inverter is used in this project. As it can be observed from Figure 3.5, the converter has six semiconductor switches and a diode in anti-parallel for each switch, which a DC-link voltage of V_{DC}. The current will flow through the anti-parallel diode when the switch oriented in the same current direction is blocked. Each two switches, together with the anti-parallel diodes form a phase leg.

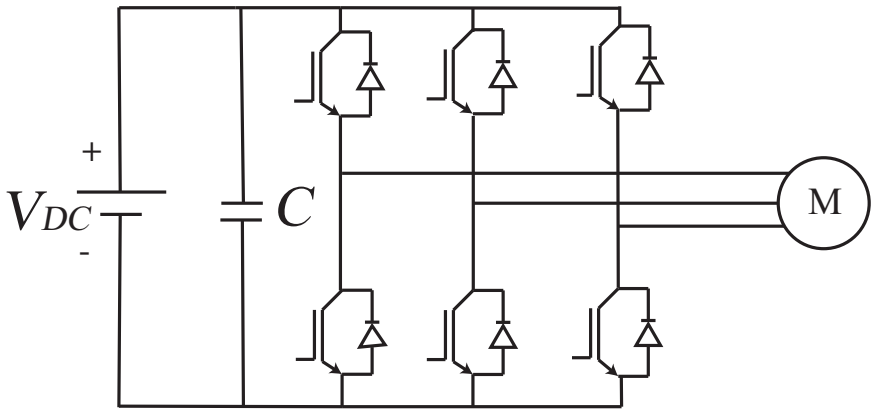

Figure 3.5: Converter Topology.

The converter is controlled through pulse width modulation. To obtain the switching pattern, one method is to use voltage references that are compared with a carrier wave, which typically is a triangular signal. The upper switch is turned on when the reference is higher than the carrier wave for the corresponding phase and vice versa. Figure 3.6 shows the reference and the carrier waves for the PWM control strategy.

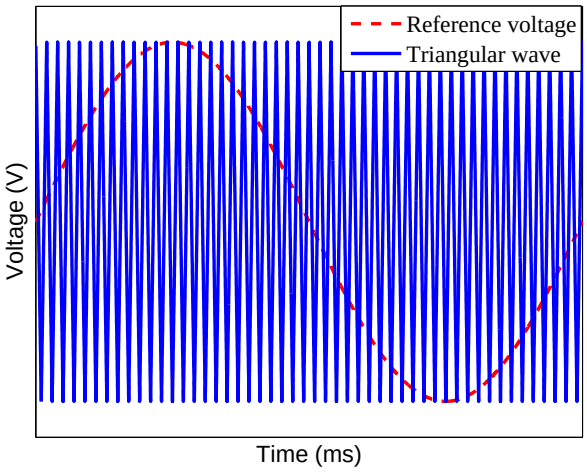

Figure 3.6: Theoretical PWM modulation waveforms.

Here, the reference wave is a sinusoidal signal, where the peak of the sine-wave is equal to the peak of the carrier wave. The peak of the phase voltage in this case becomes

$$\hat{V}_{ph} = V_{DC}/2 \tag{3.22}$$

When the reference wave has a lower magnitude, the output voltage value is also lower. By definition, M is the amplitude modulation index and is the ratio between the peaks of the reference and the carrier waves [30]. The general expression for the phase voltage then becomes

$$\hat{V}_{ph} = MV_{DC}/2 \qquad (M \leq 1) \tag{3.23}$$

If the peak of the reference wave is exceeding the peak of the carrier wave, then the modulation index would be greater than 1. At these instances the switch stays on during the whole time the magnitude of the reference wave is exceeding the magnitude of the carrier wave. This phenomenon is called over modulation. Figure 3.7 shows the reference and carrier signals for the over modulation.

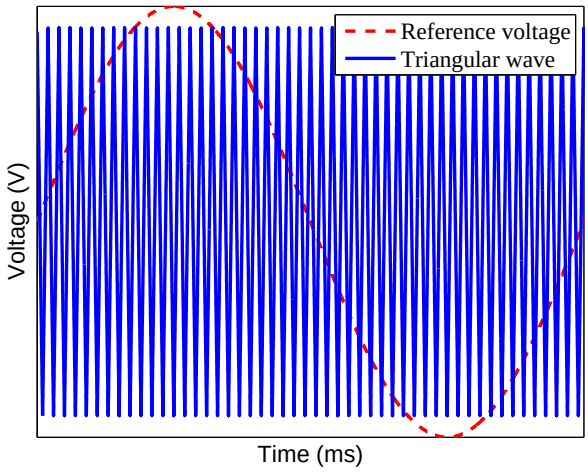

Figure 3.7: Theoretical PWM modulation waveforms with a sine wave causing over modulation.

Low frequency harmonics are created at over modulation, which are undesirable. In order to avoid over modulation, the maximum phase voltage must fulfill the requirements given in (3.23), when the modulation index is 1. Due to voltage drops in modules, blanking time as well as a control margin, modulation index can not reach 1. In order to account for these effects, the ideal DC-link to phase voltage relation is divided with a factor of 0.95. The resulting voltage relation between the DC-link voltage and the peak phase voltage needed by the generator therefore becomes

$$V_{DC} = 2\hat{V}_{ph}/0.95 \tag{3.24}$$

The conduction losses of the IGBT can be determined as

$$P_{cond_{IGBT}} = (\frac{1}{2\pi} + (\frac{M\cos(\phi)}{8}))V_T\hat{I}_1 + (\frac{1}{8} + (\frac{M\cos(\phi)}{3\pi}))R_T\hat{I}_1{}^2 \tag{3.25}$$

where $\cos(\phi)$ is the load angle, V_T is the threshold voltage and R_T is the internal resistance of the IGBT, according to [31]. $\hat{I}_1$ is the peak current value. The modulation index for this operation is calculated as

$$M = \frac{\sqrt{3}/2U_{max}}{V_{ref}} \tag{3.26}$$

where U_{max} is the maximum value of the phase voltage. The switching losses for the IGBT is

$$P_{sw_{IGBT}} = f_{sw} E_{sw_{IGBT}} (\frac{1}{\pi} \frac{\hat{I}_1}{I_{ref}})^{k_i} (\frac{V_{DC}}{V_{ref}})^{k_v} \tag{3.27}$$

where f_{sw} is the switching frequency, k_i and k_v are exponents of the current and voltage dependency for switching loss calculation. V_{DC} is the DC-link voltage, I_{ref} and V_{ref} are the reference current and the voltage for which the switching losses are given in the datasheet, respectively. $E_{sw_{IGBT}}$ represents the total switching energy losses and is calculated as

$$E_{sw_{IGBT}} = E_{on_{IGBT}} + E_{off_{IGBT}} \tag{3.28}$$

Here, $E_{on_{IGBT}}$ is the turn on and $E_{off_{IGBT}}$ is the turn off energy loss of the IGBT for I_{ref} and V_{ref}. V_T, R_T, $E_{on_{IGBT}}$, $E_{off_{IGBT}}$ are obtained from the data sheet. k_i and k_v are selected to be 1 and 1.35 respectively [32]. The conduction losses of the diode is

$$P_{cond_D} = (\frac{1}{2\pi} + (\frac{M\cos(\phi)}{8}))V_F \hat{I}_1 + (\frac{1}{8} - (\frac{M\cos(\phi)}{3\pi}))R_F \hat{I_1}^2 \tag{3.29}$$

where V_F is the forward voltage drop and R_F is the internal resistance of the diode and both are obtained from the IGBT data sheet. The switching losses of the diode is

$$P_{sw_D} = f_{sw} E_{sw_D} (\frac{1}{\pi} \frac{\hat{I}_1}{I_{ref}})^{k_i} (\frac{V_{DC}}{V_{ref}})^{k_v} \tag{3.30}$$

Here, E_{sw_D} is the diode switching energy loss and is given in the data sheet. k_i and k_v are selected as 1 and 0.6 respectively for the diode in this project [32]. The total converter loss is then

$$P_{converter} = 6(P_{cond_{IGBT}} + P_{sw_{IGBT}} + P_{cond_D} + P_{sw_D}) \tag{3.31}$$

where a factor of 6 is used since there are six switches in the converter.

In order to utilize the DC-link voltage more effectively, the zero sequence signal injection method can be used. Addition of the zero sequence signal does not effect the machine operation, since the machine neutral point is not connected so that the line to line voltages remain sinusoidal. Using this method, the reference voltage signal is altered from the sine-wave. Here, the third harmonic injection method is used, which is one way to execute the zero sequence signal injection [33]. Figure 3.8 shows the PWM modulation with third harmonic injection, using the same line to line voltage magnitude as in Figure 3.7.

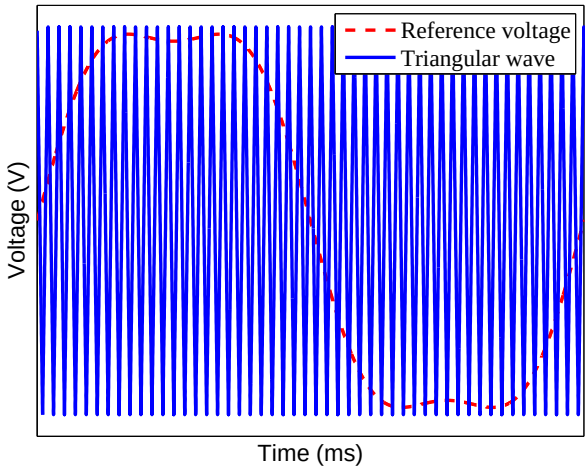

Figure 3.8: Theoretical PWM modulation waveforms using the zero sequence signal injection method.

It can be observed that the reference signal is no longer exceeding the triangular wave. The DC-link voltage required to handle this operation is

$$V_{DC} = \sqrt{3}\hat{V}_{ph}/0.95 \tag{3.32}$$

which is approximately 15% higher than the pure sine-wave modulation. The conduction losses for this case are slightly modified and are [33]

$$P_{cond_{IGBT}} = (\frac{1}{2\pi} + (\frac{M\cos(\phi)}{8}))V_T\hat{I}_1 + (\frac{1}{8} + (\frac{M\cos(\phi)}{3\pi}) - \frac{(1/6)\cos(3\phi)}{15})R_T\hat{I}_1{}^2 \tag{3.33}$$

where $\frac{1}{6}$ represents the magnitude of the third harmonic signal injection. The diode conduction losses are updated similarly and are

$$P_{cond_D} = (\frac{1}{2\pi} + (\frac{M\cos(\phi)}{8}))V_F\hat{I}_1 + (\frac{1}{8} - (\frac{M\cos(\phi)}{3\pi}) + \frac{(1/6)\cos(3\phi)}{15})R_F\hat{I}_1{}^2 \tag{3.34}$$

Chapter 4

Case setup

4.1 Wave Model

4.1.1 Wave Data and Wave Energy

The statistical representation of sea states consisting of irregular waves was explained in Chapter 2. However, in this project, the sea is assumed to have only single frequency sinusoidal waves and the distribution of these waves with regards to their probability of occurrence is given in Table 4.1.

Table 4.1: Probability of occurrence for different wave height and wave period combinations for single frequency sinusoidal waves.

H/T	3.75	4.25	4.75	5.25	5.75	6.25	6.75	7.25	7.75	8.25	SUM
0.75	0	0.4	1.2	1.6	1.1	0.7	0.2	0	0	0	5.3
1.25	0.1	4.9	5.7	6.2	4.6	4.3	1.2	0.3	0	0	27.3
1.75	0	0.7	6.1	9.6	7.3	5.2	2.2	0.8	0.1	0	32
2.25	0	0	0.1	3.2	6.7	5.1	1.6	0.7	0.3	0	17.7
2.75	0	0	0	0.1	2.4	5	1.1	0.6	0.2	0.1	9.4
3.25	0	0	0	0	0.1	1.6	1.7	0.7	0.6	0.2	5
3.75	0	0	0	0	0	0.1	0.9	0.5	0.3	0.1	2
4.25	0	0	0	0	0	0	0	0.5	0.3	0.1	0.9
4.75	0	0	0	0	0	0	0	0	0.3	0.1	0.4
5.25	0	0	0	0	0	0	0	0	0	0.1	0.1
SUM	0.1	6	13.1	20.8	22.1	21.9	8.8	4.3	2.1	0.6	100

This distribution is used in order to determine an electric power profile to be used for design purposes. Using (2.13), the available wave power is shown in Figure 4.1 for different $H - T$ combinations.

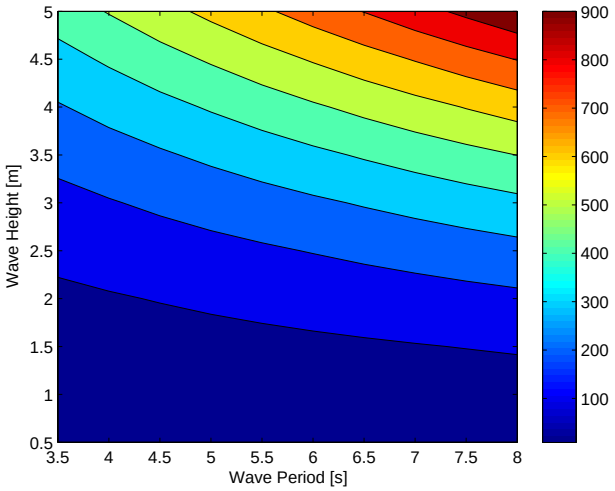

Figure 4.1: Available wave power in kW/m as a function of wave height and period.

As expected from (2.13), for higher $H - T$ values, the available power in the wave increases.

By combining Table 4.1 and Figure 4.1, the probability of achieving different available power levels can be obtained. Figure 4.2 shows the individual probability of occurrences for each different combination from Table 4.1 with regards to the available wave power. As it can be observed, lower H and T combinations are more common, whereas the very high $H - T$ combinations have a very low probability of occurrence.

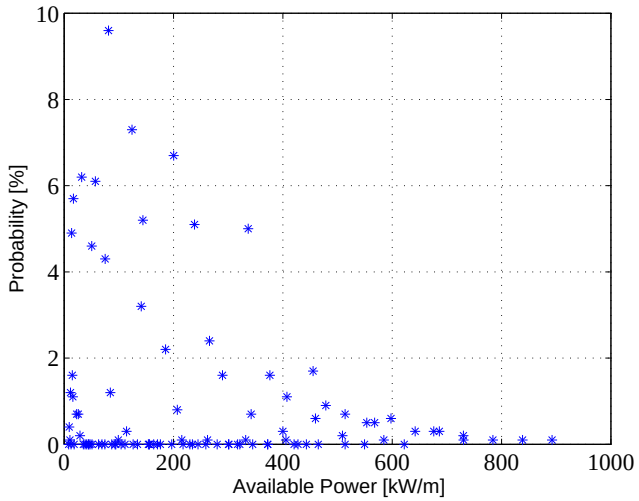

Figure 4.2: Probability mass of the Karmöy Location.

Figure 4.3 shows the probability mass distribution of different combinations from the scatter diagram. It can be observed that the most probable peak output power is approximately 150 kW/m while the peak output power can reach up to 900 kW/m. It can be seen from the figure that the probability of occurrence of this value is very low.

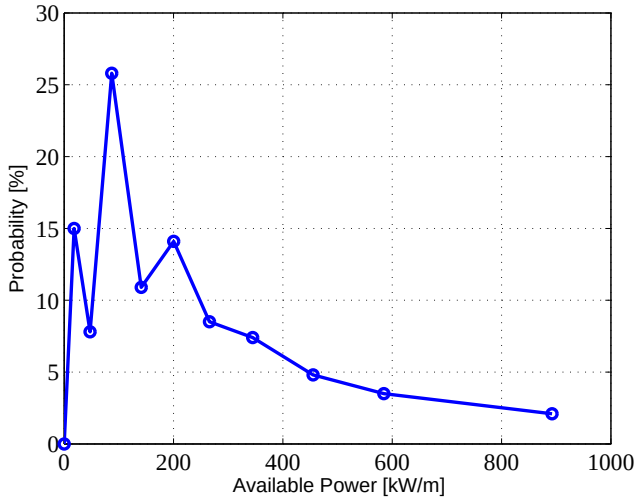

Figure 4.3: Probability mass distribution of the Karmöy location.

Figure 4.4 shows the cumulative distribution function (cdf) of this scatter

diagram. It can be seen that the slope of the curve is quite low for the high power levels, since the high power waves seldom occur.

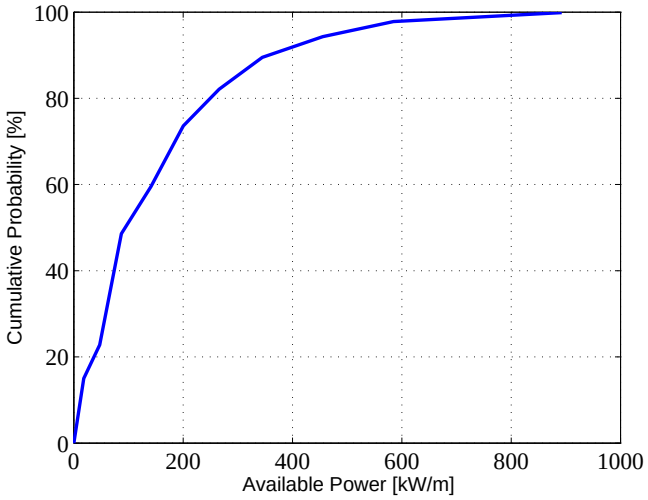

Figure 4.4: Cumulative Distribution Function of the Karmöy Location.

The available wave energy is calculated through (2.12) and is shown in Figure 4.5.

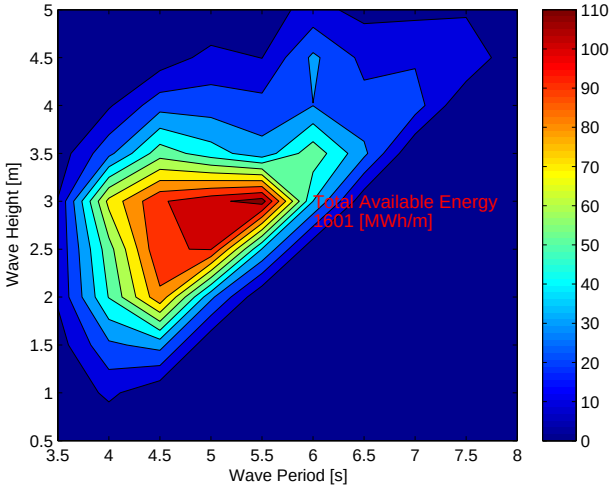

Figure 4.5: Annual Available Wave Energy in Mwh/m.

It can be observed that the annual available wave energy is $1601 MWh/m$ and the highest energy production does not correspond to the highest power

values, since the probability has a very important impact on the annual energy distribution.

4.1.2 Optimal Buoy Sizing

As mentioned before, the buoy is to be dimensioned for a certain wave environment. With the knowledge of the distribution of different wave heights and wave periods, the optimal buoy radius can be investigated, in order to obtain the highest amount of energy. Figure 4.6 shows the total energy obtained in a year by a single buoy for different buoy radii.

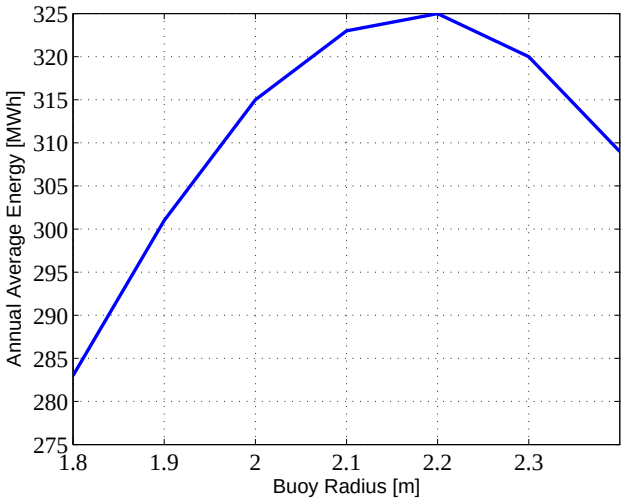

Figure 4.6: Variation of the total annual energy for different buoy sizes.

According to this figure, maximum energy is harnessed with a 2.2 meter buoy radius. Therefore the point absorber used in this thesis will have a 2.2 m radius and the forthcoming results in this chapter are obtained with the mentioned geometry. The vertical length of the buoy is selected to be 10 meters. The water depth is selected as 50 meters.

4.1.3 Modelling and Simulation of the Point Absorber in Regular Waves

Table 4.1 states that the most probable H and T combination is 1.75 m and 5.25 seconds respectively, therefore this combination is used in the coming section while simulating the point absorber dynamics.

Figure 4.7 shows the forces acting on the buoy. It can be observed that the buoyancy force is the dominating force and the rest of the counteracting forces are cancelled out, which is expected to ensure the regular floatation of the point absorber.

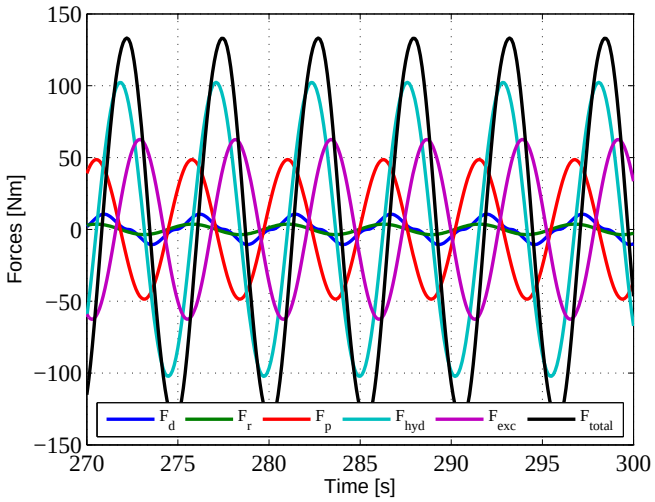

Figure 4.7: Hydrodynamic forces acting on the 2.2 m buoy for H=1.75 and T=5.25.

The forces that are shown in figure 4.7 determine the buoy movement. Figure 4.8 shows the corresponding buoy movement together with the wave elevation. The reference point for the buoy movement is the gravitational center of the buoy.

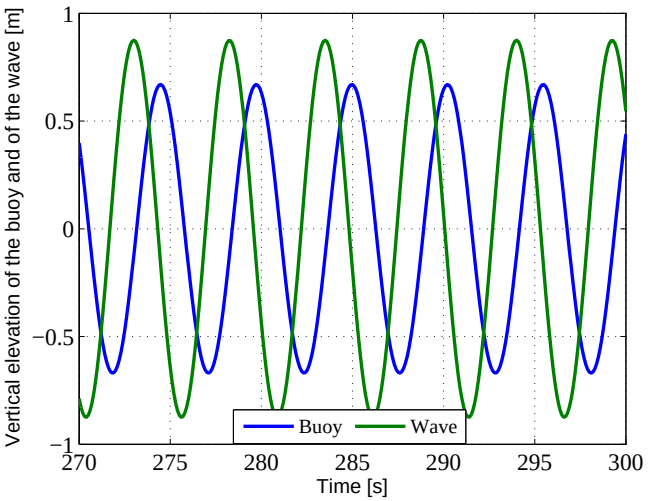

Figure 4.8: Wave elevation and the corresponding buoy movement.

The power converter through this WEC for the H and T indicated above is shown in Figure 4.9.

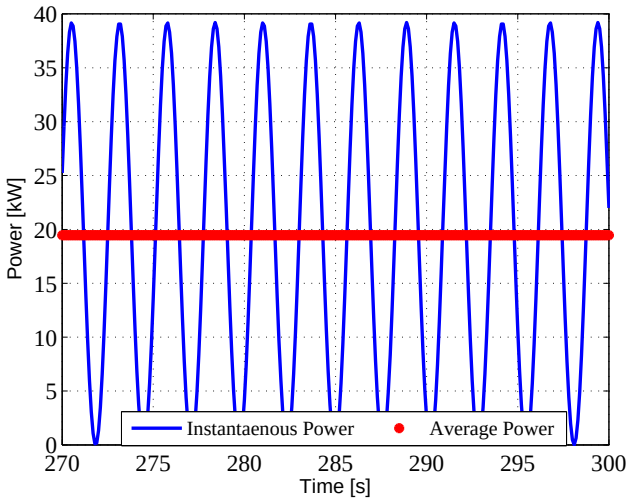

Figure 4.9: Instantaneous and the Average power from the WEC for the most probable wave.

Due to the sinusoidal form of the regular waves, the peak power output is twice the average. Furthermore, since power is captured for both positive and negative buoy movement, the frequency of the output power is the double of the wave frequency.

4.1.4 Power Output and Energy Generation of the WEC

After calculating the available wave energy and having presented the WEC operation, here the annual power and energy profiles of the WEC for the whole range of wave heights and periods are investigated to be able to have a better understanding of the electrical system requirements. The annual average and peak power distributions of the WEC placed at the mentioned location is shown in Figure 4.10.

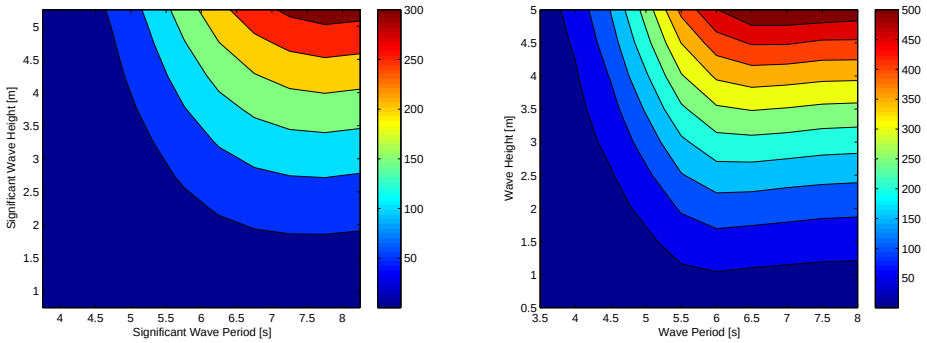

(a) Average Power. (b) Peak Power.

Figure 4.10: Average and Peak Power Outputs

It can be seen that the highest average power obtained from the generator is 300 kW. The annual energy distribution of the same location can be seen in Figure 4.11. As expected, the energy distribution is consistent with the probability of occurrence and the total possible annual energy to extract is calculated to be 325 MWh.

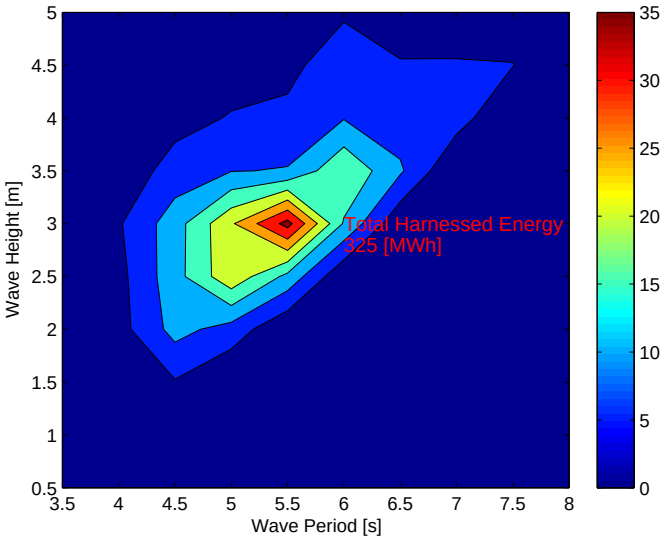

Figure 4.11: Average energy from the WEC per year.

According to the results above, the electrical system is now to be designed for the highest peak power output from the WEC.

4.2 Power Curtailment

As mentioned previously, the electrical system is to be designed for the highest peak power, yet Figure 4.3 shows that the wave conditions that give the highest power have low probability of occurrence. Full power dimensioning of the electrical system in order to accommodate the high power, low probability waves would increase the system cost substantially. Therefore, it might be more beneficial to curtail the power at a suitable level, in order to decrease the size of the WEC system. The design criteria is the instantaneous peak power from the power extraction unit.

Figure 4.12 shows the energy loss in percentage for different power curtailment levels.

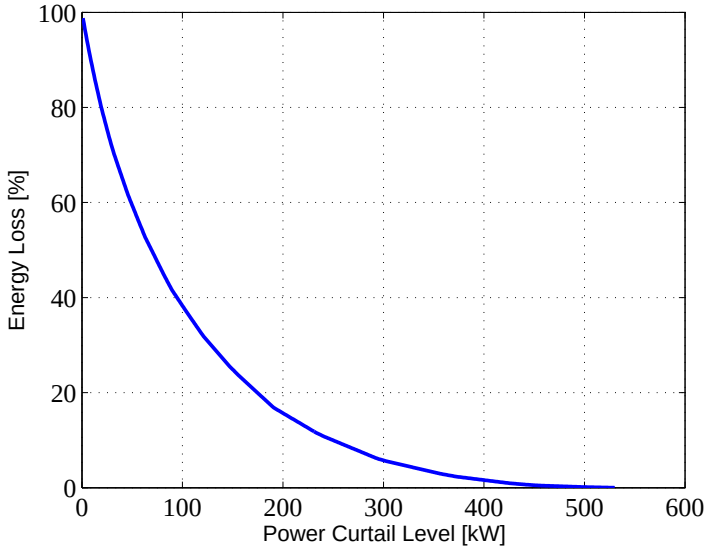

Figure 4.12: Energy loss in percentage according to the power curtailment level.

It can be seen that even when the power is curtailed approximately 50%, only 10% of the total energy is lost. Figure 4.13 shows the annual total energy for different power curtailment levels, using absolute numbers.

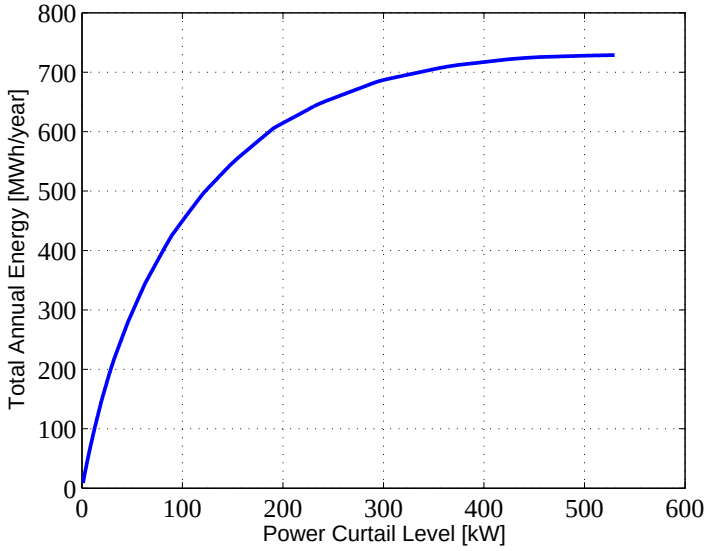

Figure 4.13: Total energy for the corresponding the power curtailment level.

4.3 Mechanical Conversion and Torque Determination

4.3.1 Linear to Rotating motion and Gearing Ratio

Based on the power curtailment investigation, the absolute electromagnetic level for the system design is chosen to be 250 kW. However, as is seen from Figure 4.10(b) this power level can be achieved at different sea conditions. Figure 4.14 shows the power extraction force as a function of the buoy speed for different $H - T$ combinations, all corresponding to 250 kW peak power.

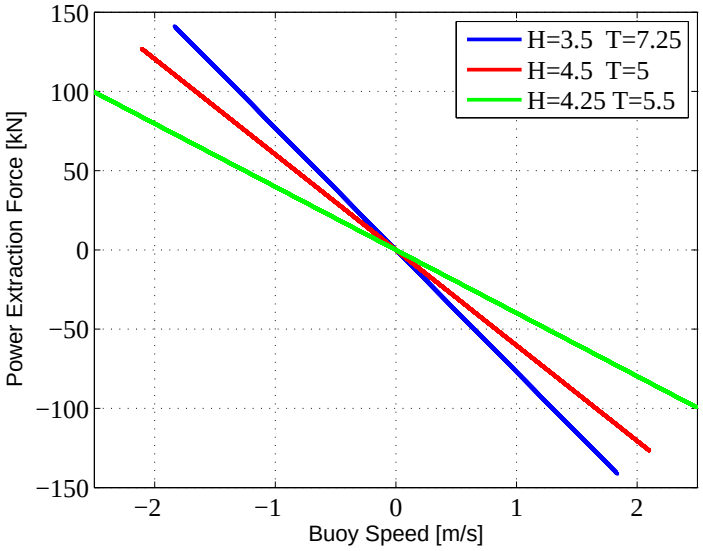

Figure 4.14: Force vs buoy speed for different H-T combinations for the same power level.

As it can be observed, the force-speed curves have different slopes for the same power output. This is due to the fact that each $H - T$ combination has different power extraction coefficient optimal for that level. The gearbox ratio is selected to be 171, which is suitable for the most occurring $H - T$ combination which provides 250 kW.

As mentioned, the generator power is selected to be 250 kW and the rotor speed of the machine is selected to be 3000 rpm. The mechanical torque of the machine will therefore be

$$T = P/\omega \tag{4.1}$$

According to above, the electric generator is designed to operate for maximum 800 Nm torque, for 3000 rpm rated speed, which correspond to 250 kW rated power. This value is the peak electromagnetic ability of the generator, however due to the sinusoidally shaped instantaneous power, the continuous power level would be half of the peak power value, without using the power curtailment. For the curtailed peak power, the continuous power level will be higher than half of the peak value, due to the chopped wave-form.

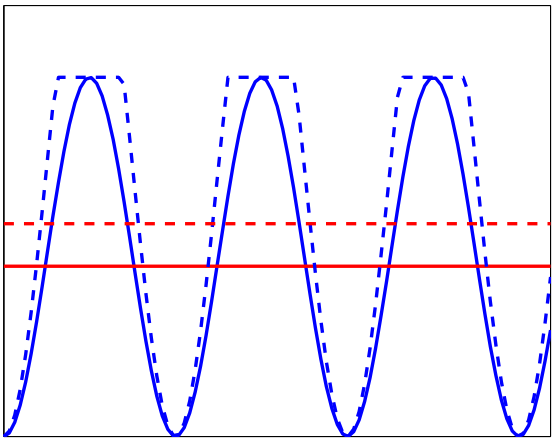

Figure 4.15: Representation of instantaneous and average power levels for non-curtailed and curtailed cases.

Here, the solid line is the non-curtailed and the dashed line is the curtailed case. It can be seen that the average level for the curtailed case is higher as expected.

4.4 Permanent Magnet Machine Design and Control

The electric machine used in this project is an interior mounted permanent magnet machine with double layer winding and two parallel branches for the windings. It is based on the Toyota Prius machine [34], with higher power output, thinner stator yoke and a two layer winding. There are 8 poles created by two-piece magnets for each pole. The electric frequency of the machine is

$$f_{el} = f_{mech} n_p = n_s n_p / 60 \tag{4.2}$$

where f_{mech} is the mechanical frequency, n_p is the number of pole pairs and n_s is the synchronous speed in rpm.

Figure 4.16 shows the initial machine design used in this project.

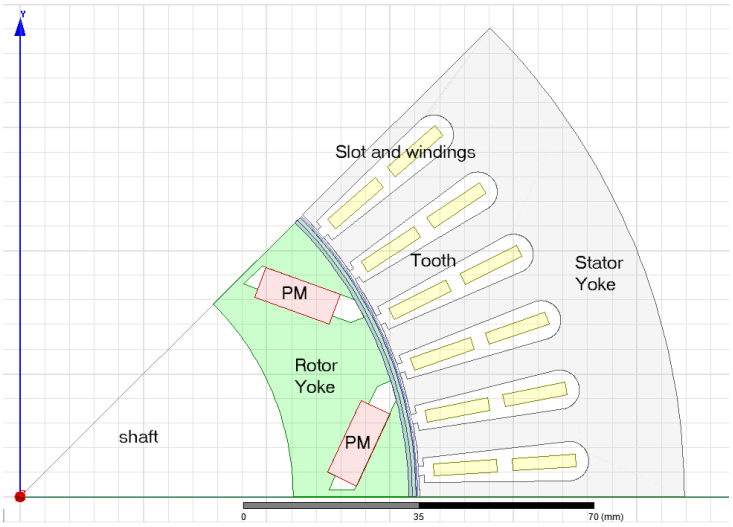

Figure 4.16: The initial machine design.

The outer stator radius of the generator is 270 mm and the active length is 260 mm. The air gap is set to be 1.5 mm. Detailed machine data can be seen in Appendix A.

4.4.1 Windings and Magnets

The rotor of this machine involves 16 permanent magnets, each couple creating a pole, resulting in 8 poles. The magnet material chosen is NdFeB and magnets are interior mounted. The relative permeability of the magnet material is 1.03. The magnet placement for one pole can be seen in figure 4.16. The stator of this machine has 48 slots, each containing a double layer winding. The total number of turns of each slot is 8. The iron material chosen for the rotor and stator construction is $M19\_29G$ [35]. The A phase coil is placed as is seen in Figure 4.17, as well as the d-axis of the generator. By aligning these two for $t = 0$ during FEM simulations, the current vector to achieve the MTPA operation can easily be implemented.

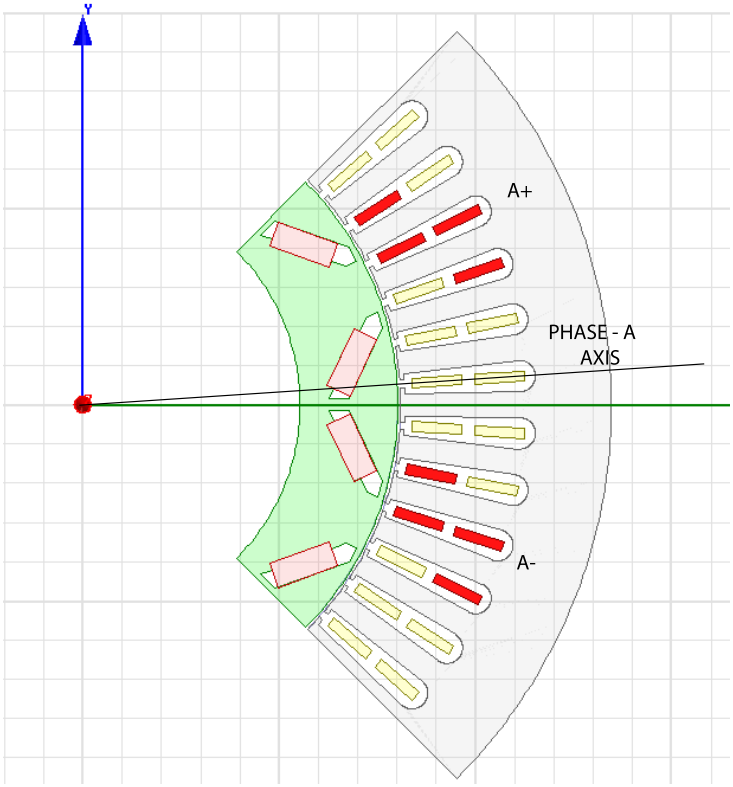

Figure 4.17: Phase A distribution of the machine.

The phase currents are set as

$$i_a = I_{max}\cos(\omega_r t + \varphi) \tag{4.3}$$

$$i_b = I_{max}\cos(\omega_r t + \varphi - \frac{2\pi}{3}) \tag{4.4}$$

$$i_c = I_{max}\cos(\omega_r t + \varphi + \frac{2\pi}{3}) \tag{4.5}$$

where I_{max} is the peak value of the current and φ is the current angle.

The maximum current is set to be 350 A for the peak power operation.

As mentioned, the stator windings are double layer windings and each layer has 4 turns. The total copper area of one layer is $32mm^2$. The area of a copper conductor then becomes

$$S_{cu} = S_{coil}/N \tag{4.6}$$

where S_{coil} is the total are of the coil and N is number of turns. The copper area in this case is 8 mm^2. It is also known that there are two parallel

branches for the machine. In this way the current in a single conductor becomes

$$350/2 = 175A \tag{4.7}$$

Using these values, the current density can be calculated as

$$J = I/S_{cu} \tag{4.8}$$

The current density of the generator for the maximum operation point is calculated to be 22 A/mm^2. The rotor resistance can be calculated through

$$R = \rho_{cu}\frac{l}{S_{cu}} \tag{4.9}$$

which then can be utilized for the generator as

$$R = \rho_{cu}\frac{1}{N_{pb}}\frac{2N(l_a)(l_{ew})}{S_{cu}} \tag{4.10}$$

where N_{pb} is the number of parallel branches, l_a is the stack length and l_{ew} is the end winding length. ρ_{cu} is the resistivity of copper. For this generator, the active length for one conductor is 520 mm and the total length of the end windings for one conductor is 390 mm. The end windings are calculated as

$$l_{ew} = 2(l_{phasearc} + l_{extra}) \tag{4.11}$$

where $l_{phasearc}$ is the length of the arc between where the conductor leaves the machine frame and goes in again. l_{extra} is the axial overhang. The resistance of the machine then becomes 22 $m\Omega$.

ï»¿

Chapter 5

Analysis

5.1 Machine Analysis

5.1.1 No Load operation

In order to observe the flux created by the permanent magnets, no load simulations are initially performed. Figure 5.1 shows the flux density created by the magnet, when the input current is set to zero. It can be observed that the rib edges have a very high flux density and in this way they saturate, which is a good feature in order to force the flux to go up to the stator teeth and not only leak over the magnets.

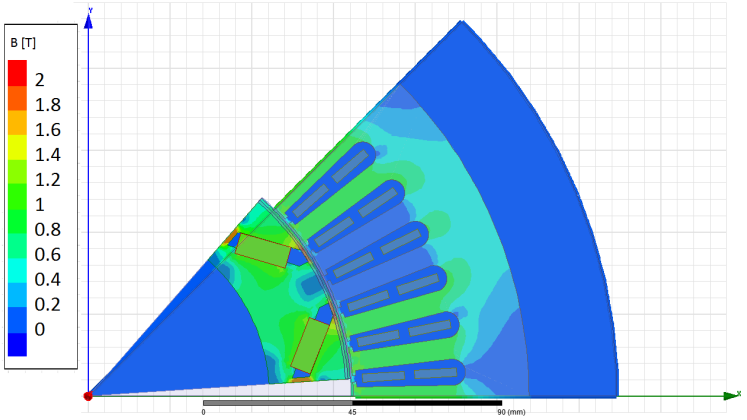

Figure 5.1: The flux density over the machine cross section for no-load operation at rated speed.

Figure 5.2 shows the flow of the flux in the machine.

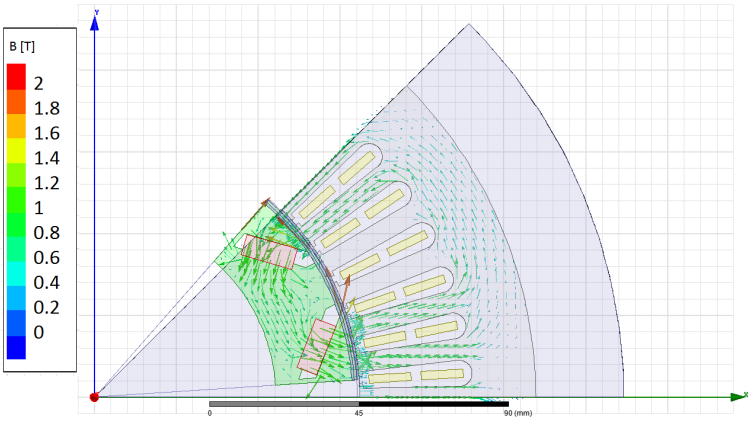

Figure 5.2: The flux density over the machine cross section for no-load operation at rated speed.

This figure verifies that the flux flows in the desired direction.

From Figure 5.3, the normal component of flux density along the air gap can be observed. The result is consistent with Figure 5.2.

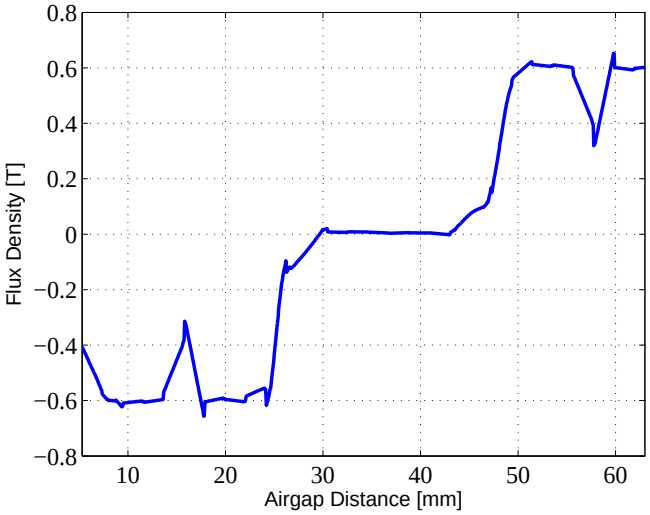

Figure 5.3: Flux density along the airgap for no-load operation at rated speed.

The airgap flux is plotted for the time 0, where the rotor is at its initial angle, as shown in Figure 5.2. The maximum air gap flux is 0.6 T, which is considered to be an adequate value [36].

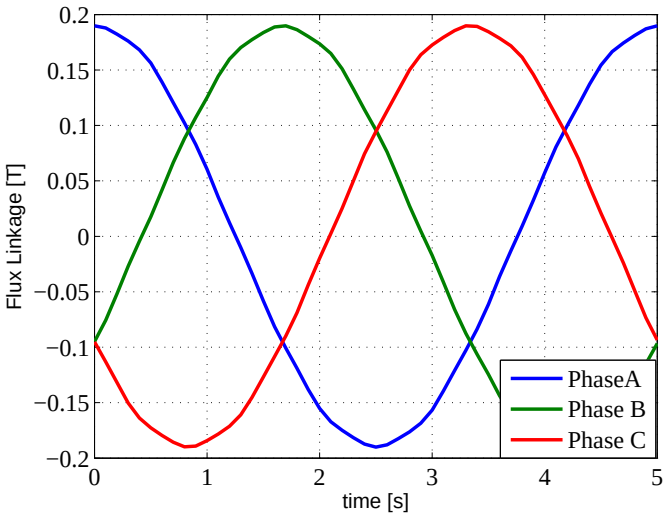

Figure 5.4: The flux linkage of stator windings for no-load operation at rated speed.

Figure 5.4 shows that the A-phase flux linkage has its maximum value at time zero, meaning that the orientation depicted in Figure 4.17 gives the desired result. The maximum flux linkage supplied by the permanent magnets at no-load operation is 0.19 Wb. Figure 5.5 shows the induced voltage of the initial generator design at rated speed.

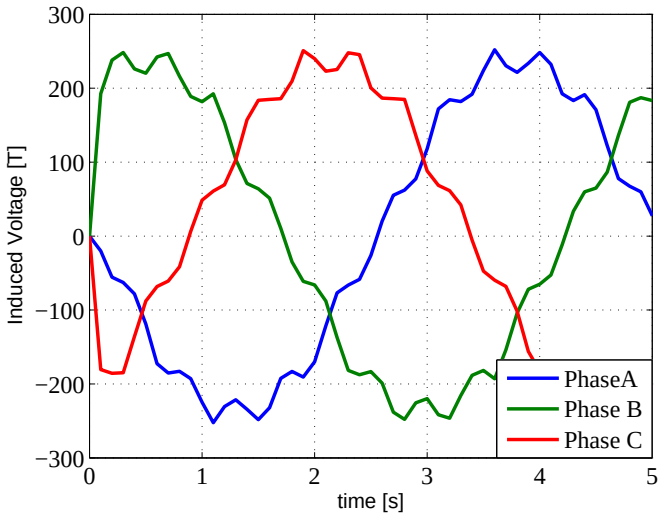

Figure 5.5: The induced voltage for no-load operation at rated speed.

5.2 Operation of the PM Generator

5.2.1 Optimal Current Angle Calculation Through FEM Analysis

Each torque and speed combination of the PMSM contributes to an operating point and a certain operating point can be achieved through various current magnitudes and angles. The Maximum Torque per Ampere (MTPA) control strategy allows us to calculate the optimal angle for any input current level in order to achieve the highest torque possible. The analytical approach in order to determine the optimal angle which gives the highest torque for the given current, with the knowledge of d-q inductances and the magnet flux linkage values. This approach can be seen in [37]. Initially these parameters are not known for the designed machine, therefore a FEM analysis or a measurement needs to be performed to establish the machine performance and the parameters.

The d-q currents are formulated as

$$i_{sd} = I_s cos(\varphi) \tag{5.1}$$

$$i_{sq} = I_s sin(\varphi) \tag{5.2}$$

where φ is the optimal angle. Figure 5.6 shows a representation of the MTPA curve for generator operation.

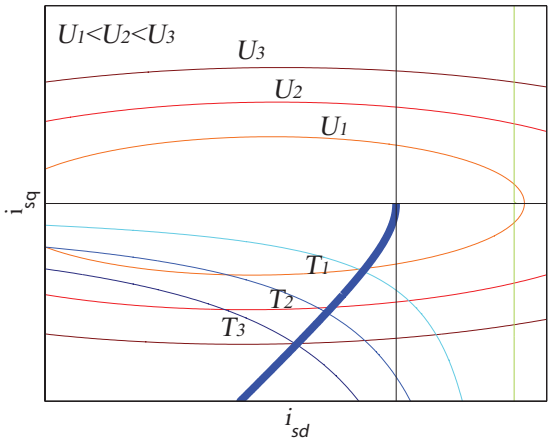

Figure 5.6: MTPA curve for generator operation in d-q current plane.

The curves marked with T are constant torque lines, determined using (3.18). As it can be observed, one torque value can be obtained by a multitude of d-q current combinations. The thick curve indicates the MTPA line. The optimal operation point is the intersection point of the desired torque line and the MTPA curve. The elliptic curves marked with U are the voltage limit lines, determined from (3.14) and (3.15), which indicate the voltage value required in order to achieve the d-q currents for the desired operation point. Accordingly, this value should be the minimum voltage level the selected converter can supply to be able to operate at all d-q current values, within the voltage ellipse. If the optimal point is not within the voltage limit, the point can not be reached. MTPA control can be utilized as long as the converter can supply the required voltage.

In this work, the optimal angle is not determined through analytical methods, but through FEM calculations. In order to calculate the optimal angle through FEM analysis, various available operating points are analyzed and the current angle which corresponds to the highest torque for a current level is the optimal angle.

Figure 5.7 shows the torque variation as a function of current angle for different current magnitudes at the rated speed. For simplicity positive notations regarding torque values and MTPA angles have been used, although they in reality are negative due to the generator operation.

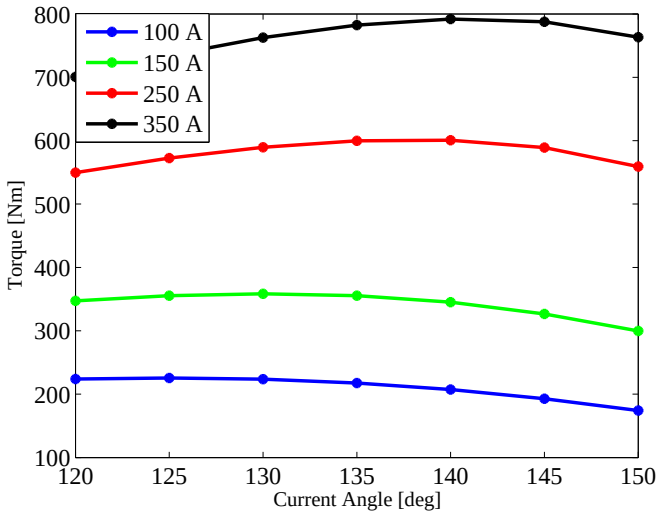

Figure 5.7: Torque variation in regards with the current angle for different current levels.

It can be observed that for low current magnitude values, the highest

torque is achieved for lower angles and while the current magnitude is increasing, the optimal angle increases as well. Figure 5.10(a) shows the d-q current combinations for different operation points and Figure 5.10(b) shows the resulting induced voltage. As before, positive torque and angle values are used for simplicity.

5.2.2 Analysis of the WEC System

In this section, the WEC is connected to the electric generator. Figure 5.8 shows the calculation procedure of the integrated WEC and electrical system.

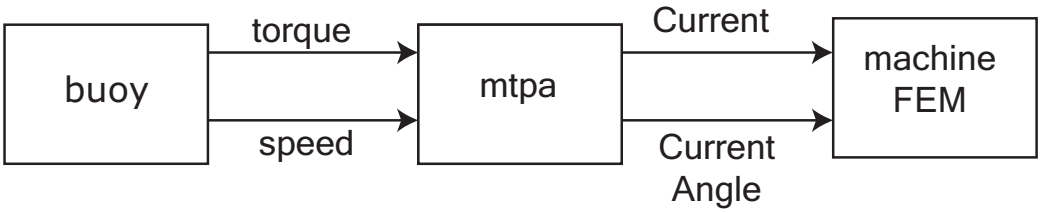

Figure 5.8: The procedure description.

Here, the simulation of the buoy movement on the water provides operating points to the electrical system, where the suitable current magnitude and angle is calculated through MTPA control for each input and the machine is analysed for this case. Figure 5.9 represents the torque input supplied to the machine by the buoy.

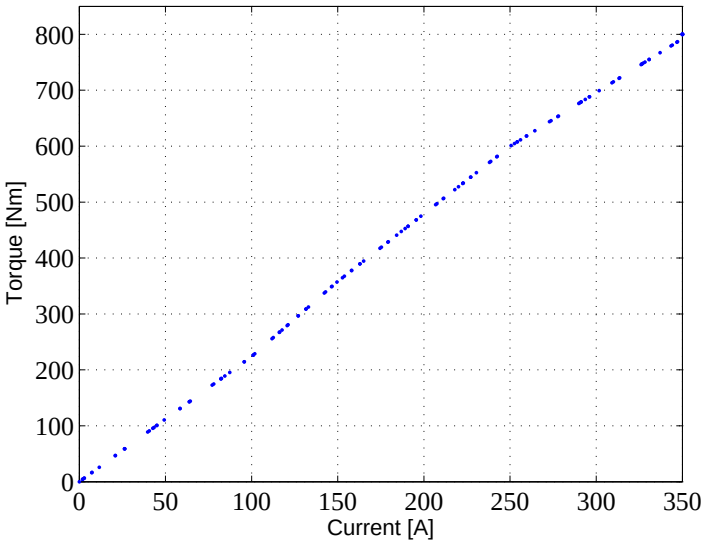

Figure 5.9: Torque and speed requirement from the buoy.

Since the load characteristic of the buoy is linear, the speed increases linearly with the torque and reaches 3000 rpm for the rated torque. Figure 5.10(a) shows the optimal d and q currents obtained through the MTPA system.

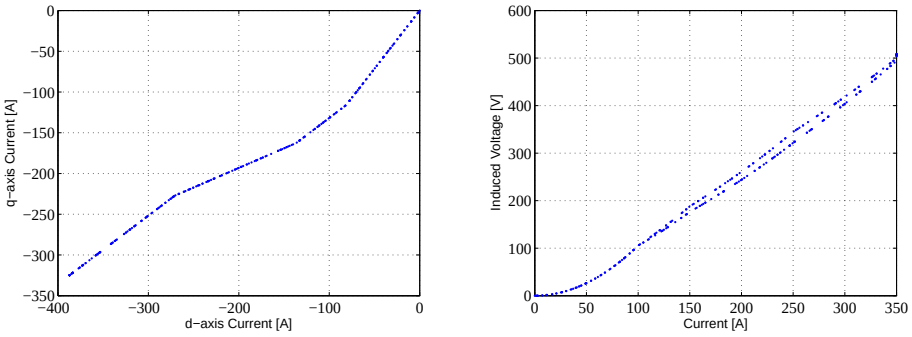

(a) Current. (b) Voltage.

Figure 5.10: Optimal d-q current trajectories and the induced voltage.

The maximum current depicted here is the instantaneous peak current. However due to the power curtailment, the continuous current of the generator will be lower. Figure 5.11 shows the relation between the peak and the continuous currents for the maximum operation point.

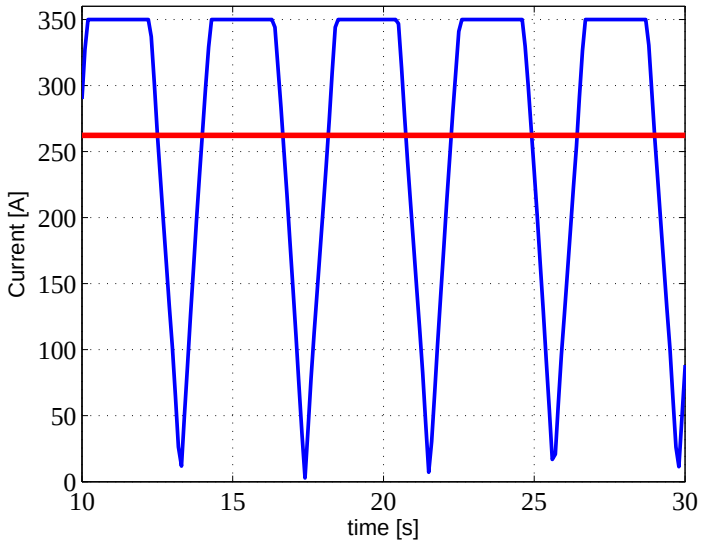

Figure 5.11: Instantaneous and the continuous currents.

The continuous current value is calculated to be 262 A whereas the peak current is 350 A. The current density for continuous current becomes 16.4 A/mm^2.

The maximum voltage is used for the converter selection. It is found that the maximum phase voltage is 506 V. This results in the need of a DC-link voltage that is

$$V_{dc} \geq V_{ph}\sqrt{3}/0.95 = 911V \tag{5.3}$$

using the zero sequence signal injection method. According to this DC-link voltage value, the $InfineonFZ600R17KE4$ 1700 V IGBT module is selected. Further information about the module can be found in [31]. The switching frequency is selected to be 5kHz. It can be seen that there is a decent voltage margin between the needed DC voltage for the induced voltage level and the rated voltage of the IGBT module. Due to this, the converter selection is suitable for forthcoming designs, since the machine is not greatly altered, therefore drastic changes in the induced voltage level are not to be expected.

The machine losses are shown in Figure 5.12(a) and the converter losses can be seen in Figure 5.12(b). The machine losses are takes from the FEM calculations and the copper losses are also verified using (4.10). The end windings are included in the copper loss calculations. The winding temperature is selected to be 120^o and the magnet temperature is assumed to be 70^o during the calculations shown in the figures. The fact that the temperature is lower for the lower current levels have been ignored to facilitate the calcu-

lations, since the effect is the same for all investigated machine variants. The core losses are obtained through the FEM calculations and the copper losses from the FEM calculations are increased in order to account for the losses from the end windings. The converter losses are calculated as described in the previous chapter.

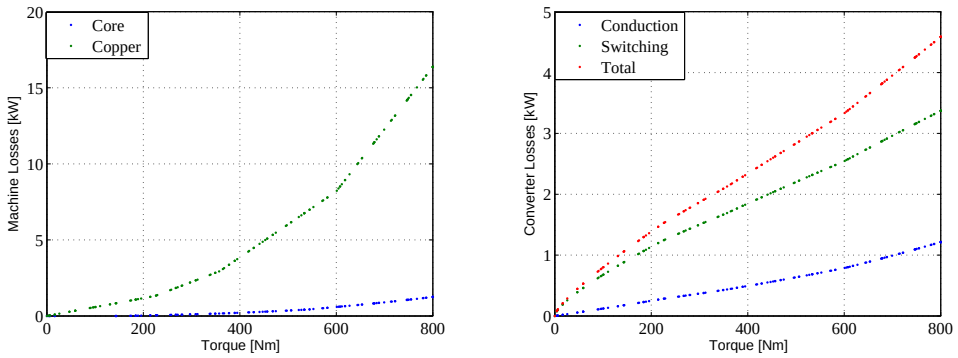

(a) Machine Losses. (b) Converter Losses.

Figure 5.12: Electrical losses of the initial WEC system.

It can be observed from above that the majority of the total losses are the copper losses, which go up to approximately 16 kW for the maximum current. In order to introduce the magnet losses in the FEM simulation, the conductivity of the magnet is introduced in the magnet representation, for details, see [38]. The magnet losses are quite small compared with the copper and the core losses, which can be expected from an interior PM machine, therefore these are not shown in the figure, however they are included in the calculations. The loss values depicted in the figures are average losses for the operation point in question. The switching losses are approximately 3.3 kW at maximum current for the 5 kHz switching frequency.

Figure 5.13 shows the temperature distribution in the generator cross section. The continuous current for the rated operation is used as an input.

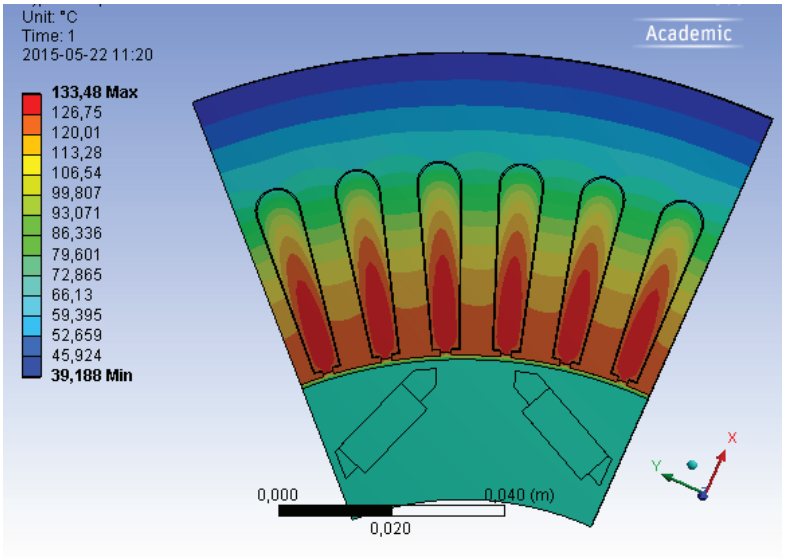

Figure 5.13: Temperature distribution in the initial generator for the maximum operating point.

The ambient temperature is selected to be 20^o. The heat transfer coefficient, α, for the machine frame side is selected to be 2000 W/m^2K and the cooling of the rotor shaft is represented with a heat transfer coefficient of 45 W/m^2K towards the shaft, which gives a rotor temperature of 70^o. It can be seen that the maximum temperature in the stator windings is slightly higher than 130^o, which corresponds to an average temperature of approximately 120^o. The temperature assumption made earlier is therefore validated through simulations.

Figure 5.14 shows the efficiency of the system for different power levels.

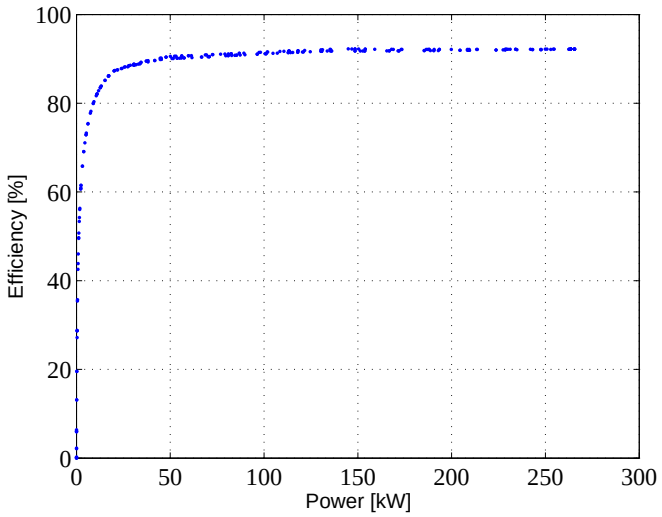

Figure 5.14: Efficiency of the initial drive system design.

It can be observed that the efficiency reaches a fairly high value of 85% at approximately 30 kW and stays fairly similar until the maximum power operation point. This means that the generator is suitable for a wave energy operation, since the efficiency is not much lower than the rated value for lower power levels. The efficiency for the rated operation is 92.2%.

5.3 Geometric Alterations

In this section, the magnet locations are altered in order to investigate the effect of the magnet placement on the electrodynamic torque. The magnet area is kept constant for each design and the magnet and the reluctance torque is calculated for the different cases.

For all sweeps, the electrodynamic torque is split into the magnet and reluctance torque components, as shown in (3.19) and the magnet and reluctance torque components are calculated using (3.20) and (3.21). The input data is obtained through FEM calculations. The magnet flux linkage is calculated as a function of the q-axis current, while the d-axis current is zero. After obtaining the magnet flux linkage, FEM calculations for different current magnitudes and angles are performed and the MTPA angle is determined for each case. The d-q inductances are calculated using (3.16) and (3.17).

5.3.1 Angular Sweep

Here, the rib and the distance from the air gap of the magnets are kept constant and the distance from the shaft is altered with an angle. The distance from the side boundaries is constant for this design, as well as the magnet volume. The geometric design for the angle sweep can be seen in Figure 5.15 where 5 designs are presented.

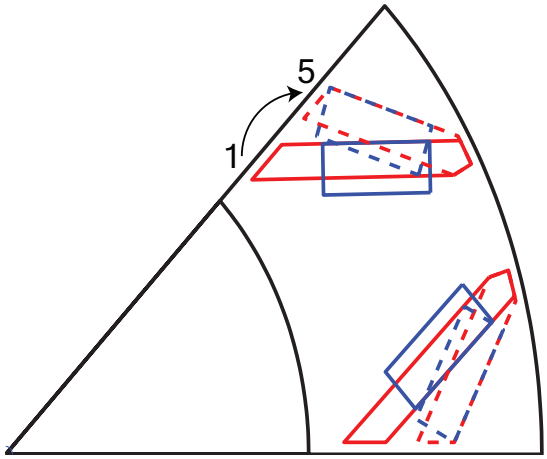

Figure 5.15: Rotor designs for the angular sweep.

The solid line represents the start design whereas the dashed line is for the end design. Altering the placement of the magnets will change the flux and accordingly the electromagnetic torque will also be effected. Figure 5.16 shows the different reluctance and magnet torques for the start and end designs.

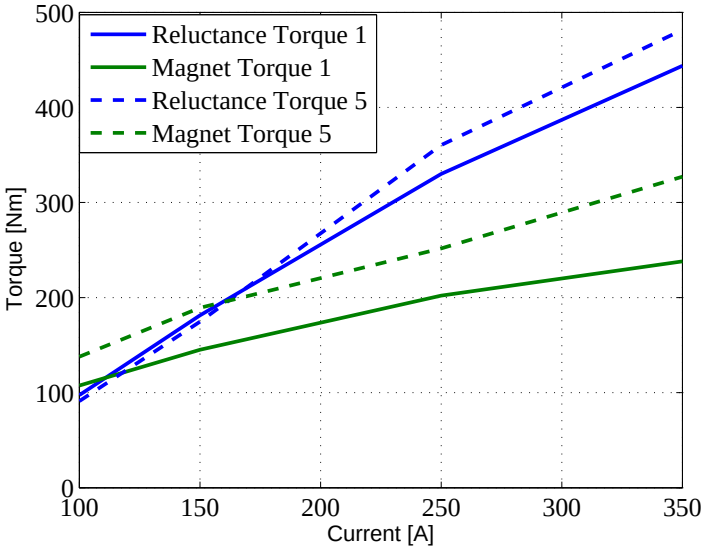

Figure 5.16: The magnet and reluctance torque variation as a function of current for the angle sweep.

It can be observed that for the start design the magnet torque is lower than that for the end design. This is due to the fact that for the start design, the magnets are placed deeper into the rotor yoke and this changes the d-q inductances, which in turn causes Ψ_m to be lower. By placing magnets closer to the air gap, the magnet torque increases. The difference between the start and end magnet torque values is approximately 100 Nm. It can also be seen that the reluctance torque increased slightly from the start to the end design. This is due to the higher difference between d and q axis inductances. Figure 5.17 shows the magnet, reluctance and electromagnetic torques for different designs.

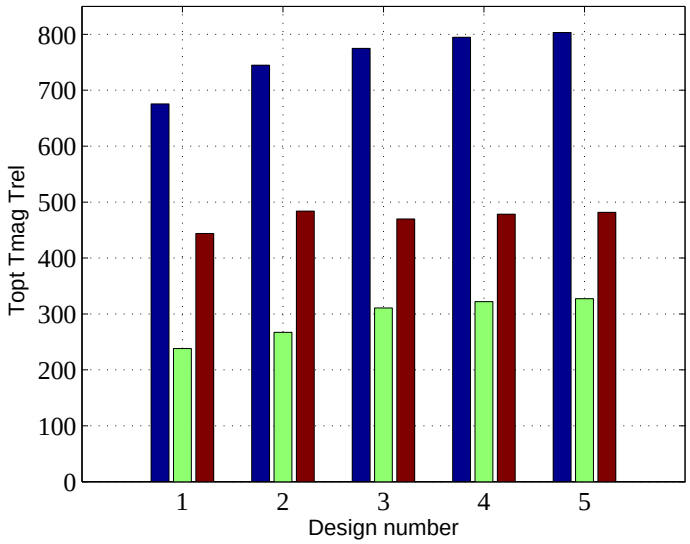

Figure 5.17: Magnet torque (green), Reluctance Torque (red) and the Total Torque (blue) for the angle sweep.

For this sweep, the highest magnet and overall torque is achieved using the 5^{th} design, however the highest reluctance torque is obtained using the 2^{nd} design.

5.3.2 Rib Sweep

In this sweep, the effect of the rib distance is investigated by reducing it. There are three designs in this sweep and for each step the magnet dimensions are adjusted while keeping the magnet volume constant. Figure 5.18 shows the geometry of different designs for the rib sweep.

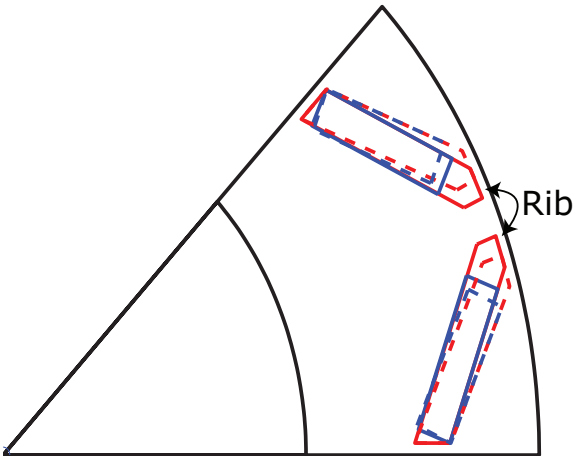

Figure 5.18: Rotor designs for the rib sweep.

The solid line represents the start design whereas the dashed line is for the end design. Figure 5.19 shows the different reluctance and magnet torques for the start and the end designs.

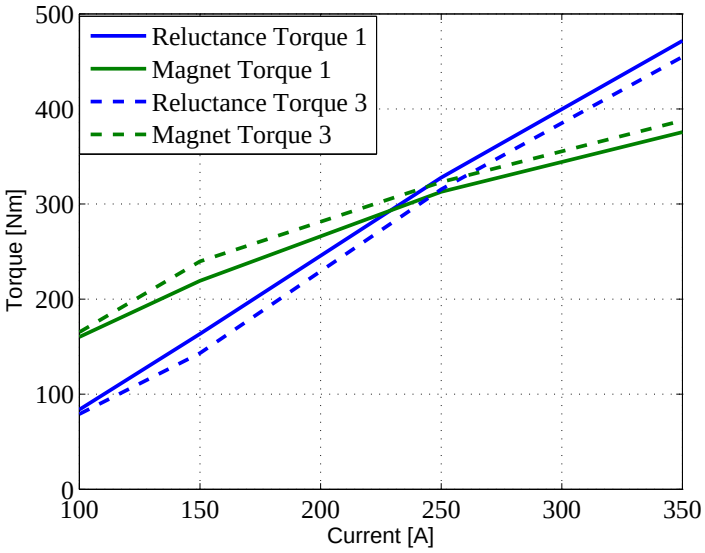

Figure 5.19: The magnet and reluctance torque variation for the rib sweep

It can be observed that with smaller rib distances, a slightly higher mag-

net torque can be achieved in comparison to the latter case. However, due to the increased saliency for the large rib distance, the reluctance torque will be higher. Furthermore, since the overall design is quite salient, the reluctance torque is higher than the magnet torque for the rated current operation. Figure 5.20 shows different magnet, reluctance and electromagnetic torques for the different designs.

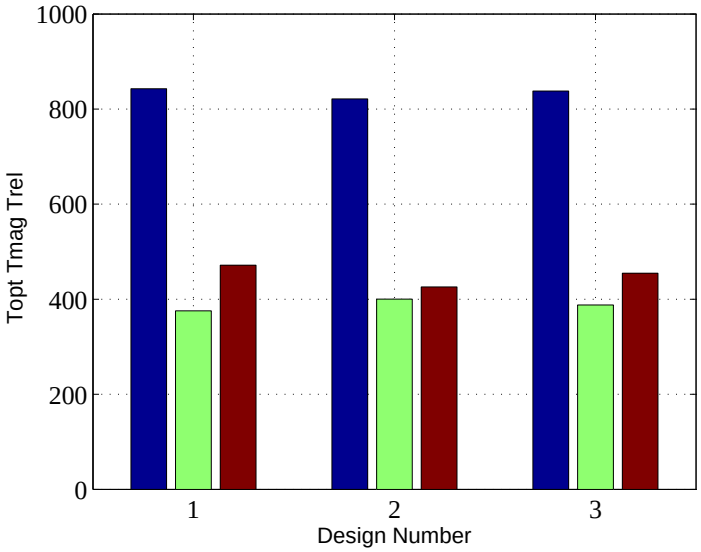

Figure 5.20: Magnet torque (green), Reluctance Torque (red) and the Total Torque (blue) for the rib sweep.

For the rib distance alterations, the highest magnet torque is obtained for the 2 nd design while the highest reluctance torque can be achieved for the 1^{st} design. However, the highest overall torque is obtained for the 3^{rd} design, since the trade off between magnet and reluctance torques is optimum for this case. It can also be noted that the rib distance has not as high impact on the torque output as the angle of the magnets.

5.3.3 Straight Sweep

In this sweep, the magnets are placed close to the air gap, with a small rib distance, which creates an inset like magnet shape. The magnets are moved towards the shaft while keeping the rib distance constant. Figure 5.21 shows the geometry of this sweep.

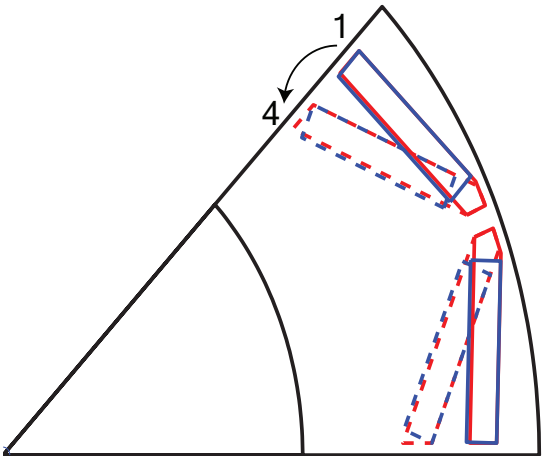

Figure 5.21: Rotor designs for the straight sweep.

The solid line represents the start design whereas the dashed line is for the end design. Altering the placement of the magnets will change the rotor flux, therefore the electromagnetic torque will also be effected. Figure 5.22 shows the different reluctance and magnet torques for the start and end designs.

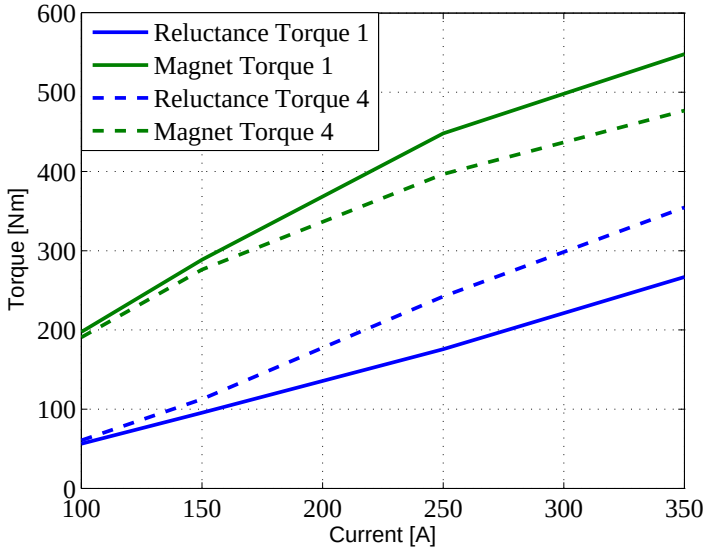

Figure 5.22: The magnet and reluctance torque variation for the straight sweep.

It can be observed that this design is not salient enough to produce high reluctance torque, therefore for the entire operation the magnet torque is higher than the reluctance torque. The magnet torque for the start design is approximately 100 Nm higher than for the end case, since the first magnet placement results in higher Ψ_m. However, due to low saliency, the start design has a lower reluctance torque than the end design. Figure 5.20 shows different magnet, reluctance and electromagnetic torques for different magnet positions in the straight sweep.

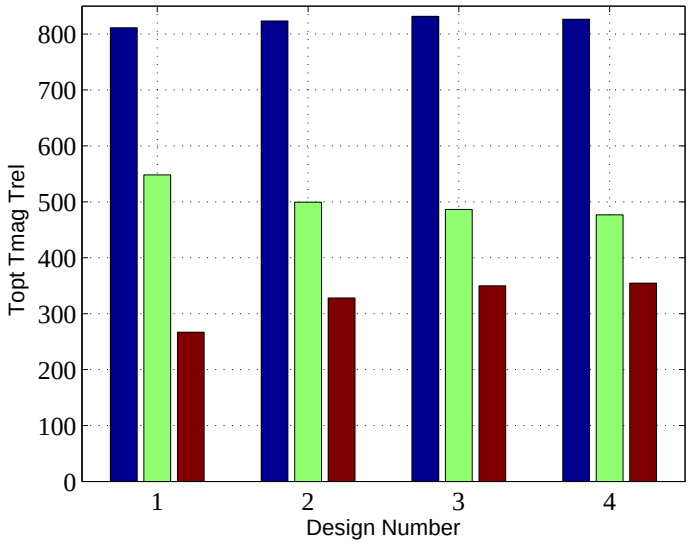

Figure 5.23: Magnet torque (green), Reluctance Torque (red) and the Total Torque (blue) for the straight sweep.

It can be observed that, due to the inverse ratio of change between the magnet and reluctance torques for different designs, the total torque is almost the same for each design. Highest magnet torque is achieved for design 1 whereas the highest reluctance torque case is design 4.

5.3.4 Spoke Magnet Desing

For this design, the permanent magnets are placed perpendicular to the air gap, similar to the structure presented in [39] and [40]. Here, three different geometries were used for the spoke design. The magnet volume is kept constant, as it was for the previous sweeps. Figure 5.24 shows the starting geometry of the spoke magnet design.

Figure 5.24: Rotor Geometry for Initial Spoke Magnet Design.

Figure 5.25 shows the flux density radially along the machine geometry. It can be seen that the flux density in the machine is coherent with the previous designs.

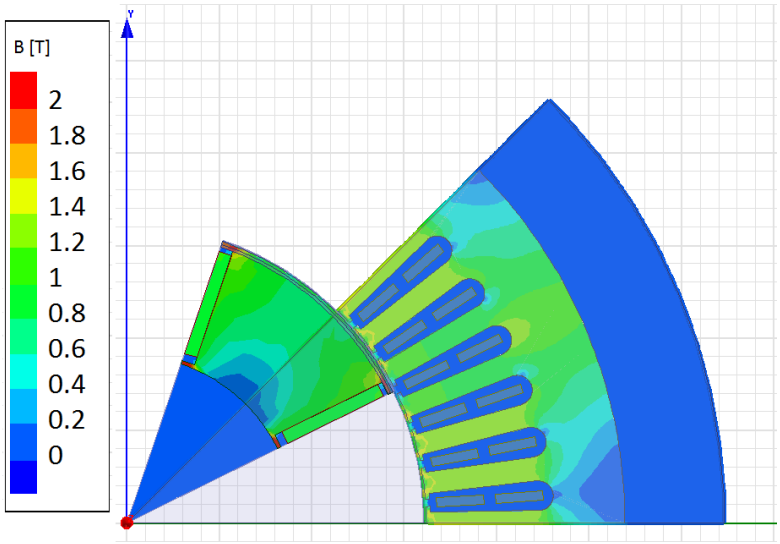

Figure 5.25: No load flux for the initial spoke magnet design.

which is similar to the initial generator design using the v-shaped magnets. For the second spoke design, two pieces of the rotor is carved out in order

to concentrate the flux over the air gap. These pieces take 17% of the outer rotor arc. Figure 5.26 shows the geometry of the second spoke design.

Figure 5.26: Rotor Geometry for Second Spoke Magnet Design.

In the third spoke design, the carved out pieces are increased to take 33% of the outer rotor arc. Figure 5.27 shows the geometry for this design.

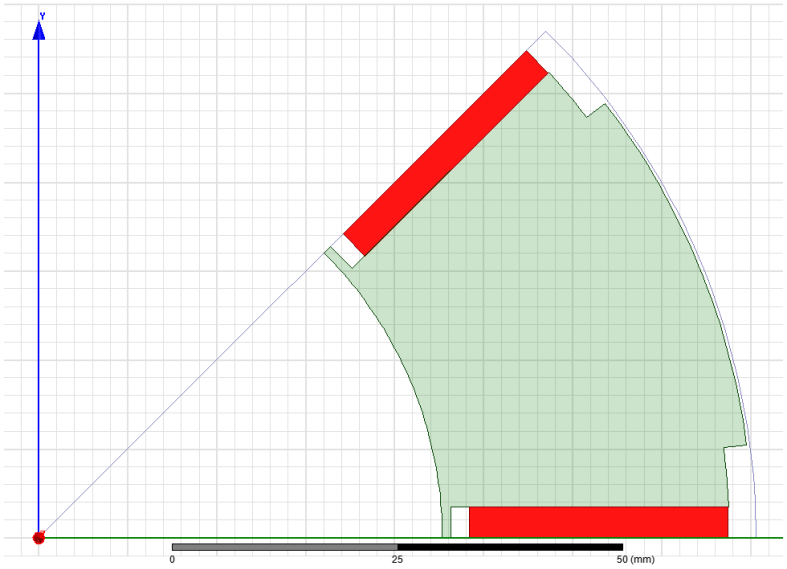

Figure 5.27: Rotor Geometry for Third Spoke Magnet Design.

Figure 5.28 shows the magnet and reluctance torque variations for the spoke design.

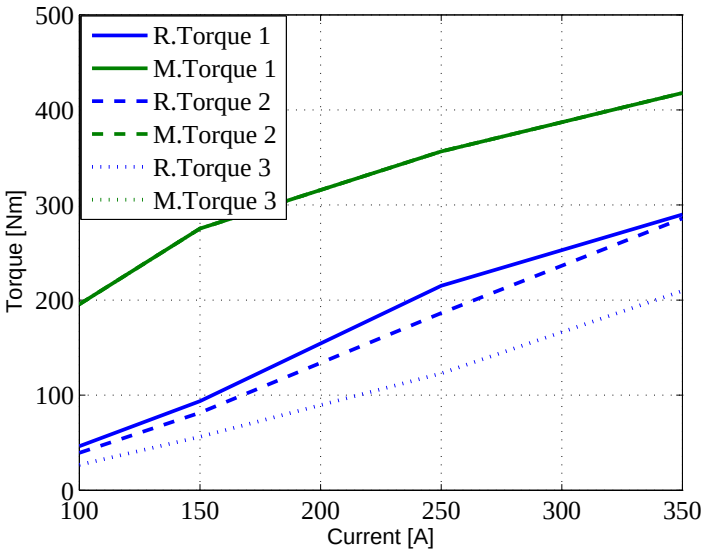

Figure 5.28: The magnet and reluctance torque variation for the spoke sweep.

It can be seen that the magnet torque is unchanged for all three cases, since the magnet placement is kept constant. On the other hand, reluctance torque decreases with the increasing size of the carved out pieces. This is due to the decreasing q-axis inductance. When the magnetic material is replaced by air, the q-axis flux linkage can not travel through the replaced bits as easily as through the iron material. Therefore the q-axis inductance decreases, which in return causes a drop in the reluctance torque value.

Figure 5.29 shows the magnet, reluctance and the total torque outputs from different spoke designs.

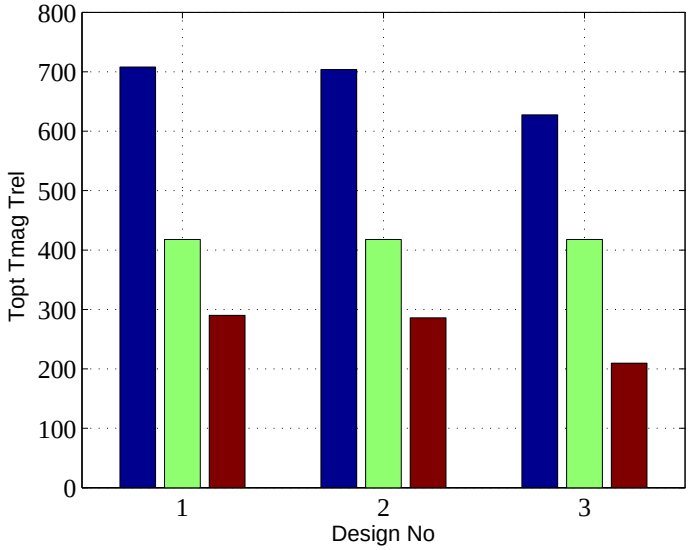

Figure 5.29: Magnet torque (green), Reluctance Torque (red) and the Total Torque (blue) for the spoke sweep.

Here, it is observed that while the magnet torque remains constant, the reluctance torque decreases from the start to the end design, in turn the total torque also decreases. It can be seen that the total torque value obtained by the spoke designs are not sufficient as a high performing generator for the investigated WEC. However, by altering the stator and increasing the magnet material, the spoke rotor generator can be a suitable option.

5.3.5 Inset Magnet Design

The inset design has a one piece magnet straight across the air gap side of the rotor. Figure 5.30 shows the geometry of the inset magnet machine. The magnet volume is kept constant just as in the previous cases. Due to modelling issues, there are two magnets with a small air pocket in between them, however, this is irrelevant for the flux picture in the machine.

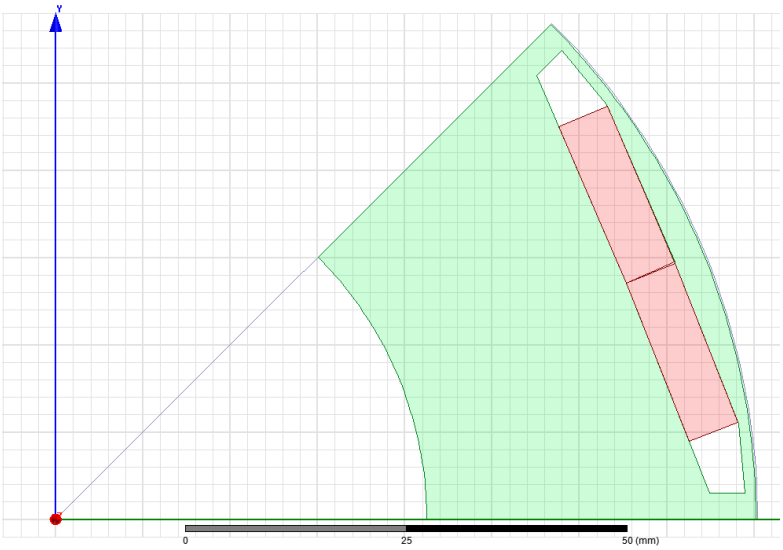

Figure 5.30: Rotor Geometry for Initial Inset Magnet Design.

Figure 5.31 shows the flux density radially along the machine for no load operation. It can be observed that the flux level of this design is within the desired values, as stated for the initial v-shaped permanent magnet generator.

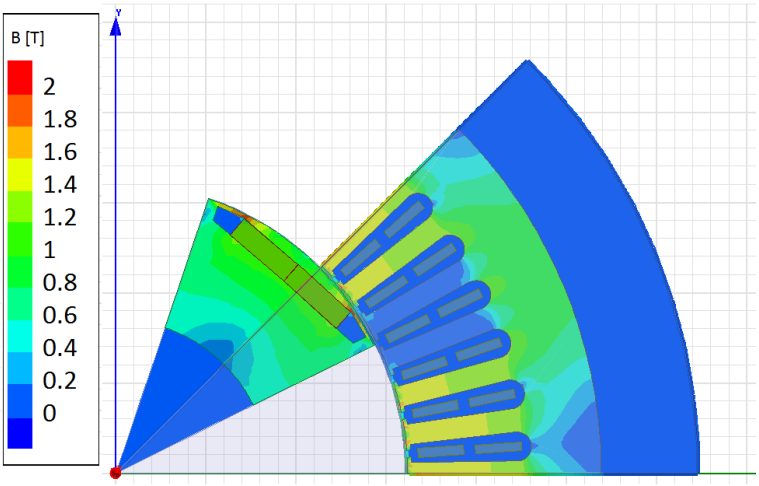

Figure 5.31: No load flux for the inset magnet design.

In order to further investigate the inset design, the magnet width is decreased while the thickness is increased to keep the volume constant. The rib is increased to be able to keep the magnet in the center of the pole. Figure 5.32 shows the rotor geometry of the second inset magnet design.

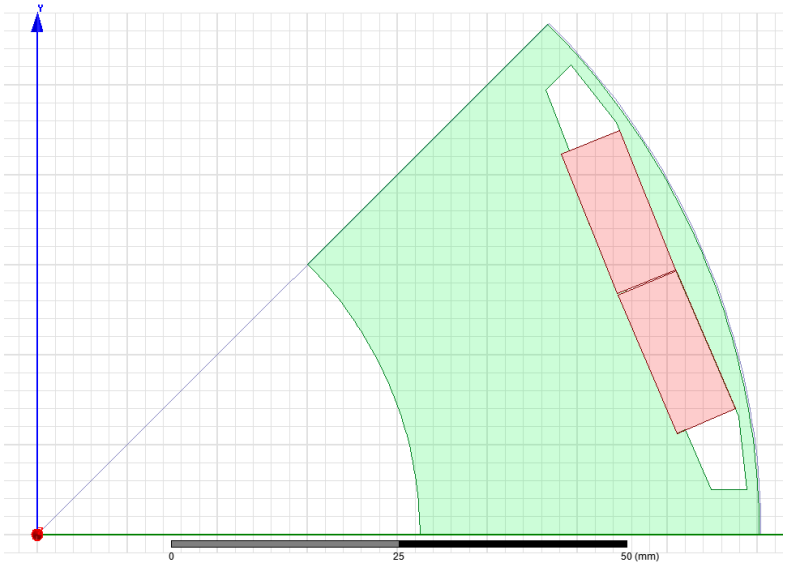

Figure 5.32: Rotor Geometry for Second Inset Magnet Design.

For the third inset magnet design, the magnet width and the rib is further decreased while the magnet volume is kept constant. Figure 5.33 shows the geometry of the third inset design.

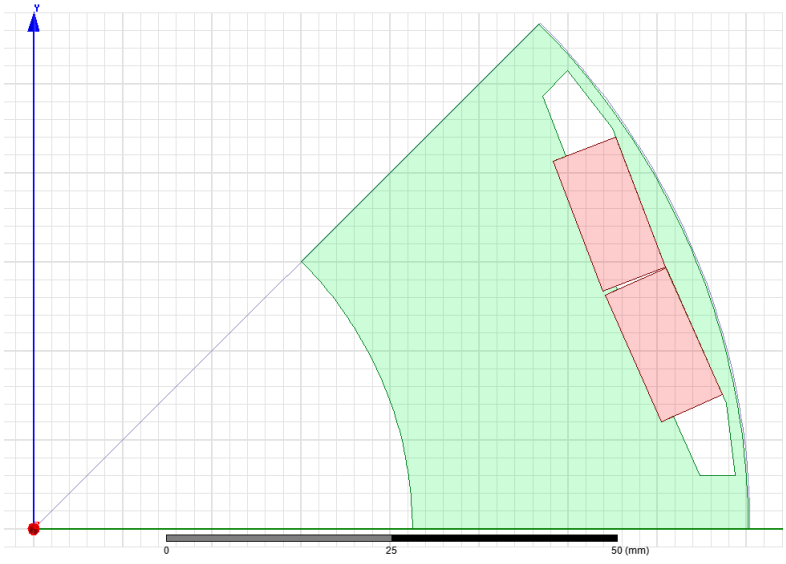

Figure 5.33: Rotor Geometry for Third Inset Magnet Design.

Figure 5.34 shows the magnet and reluctance torque variations for different inset designs.

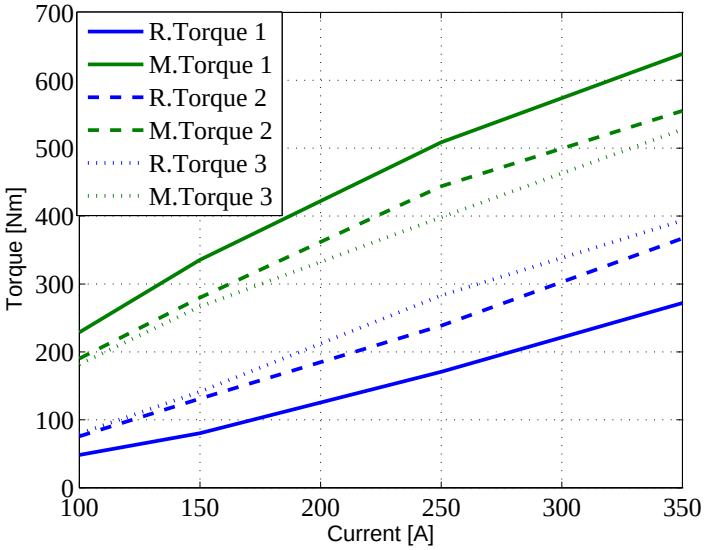

Figure 5.34: The magnet and reluctance torque variation for the inset sweep.

It is shown that the magnet torque decreases with each adjustment made from the initial to the third design. This is on account of the fact that when the magnet thickness is increased, the magnet flux needs to travel through this thicker magnet, which has a low permeability, therefore Ψ_m decreases. The lower magnet flux results in lower magnet torque. It is also observed that the reluctance torque is affected oppositely. When the magnet is long, the reluctance path for the q-axis is thinner. This gives a lower value of the q-axis inductance. By increasing the iron bits at the magnet sides, the q-axis inductance is increased. The reluctance torque is affected proportionally to the difference between d and q axis inductances, therefore it is increased from the initial to the third design. Figure 5.35 shows the magnet, reluctance and total torque values for the inset design sweep.

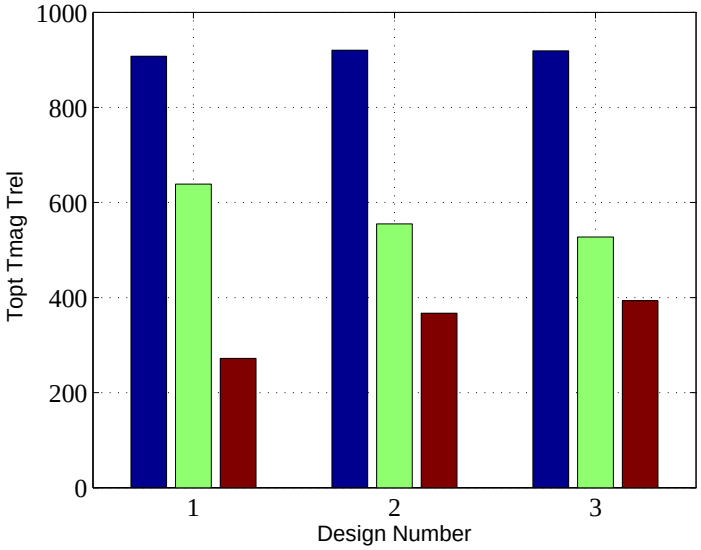

Figure 5.35: Magnet torque (green), Reluctance Torque (red) and the Total Torque (blue) for the inset sweep.

It can be seen that the total torque remains fairly constant since the reluctance and magnet torques are affected in an opposite manner by the varying inset magnet designs.

5.3.6 Evaluation

Any change in the magnet placement of the permanent magnet machine has an affect on the air gap flux and on the flux in the iron core. These deviations impact the d-q inductances of the machine. According to (3.16) and (3.17), when the d-axis flux linkage is changed, the d-axis inductance is affected, given that Ψ_m is constant for the operation point. Similarly, the q-axis flux linkage and the inductance are proportional. The effect of the geometric alterations on the d-q flux linkages are explained in the previous section.

Figure 5.36 shows the d-axis inductance variation for different sweeps and designs.

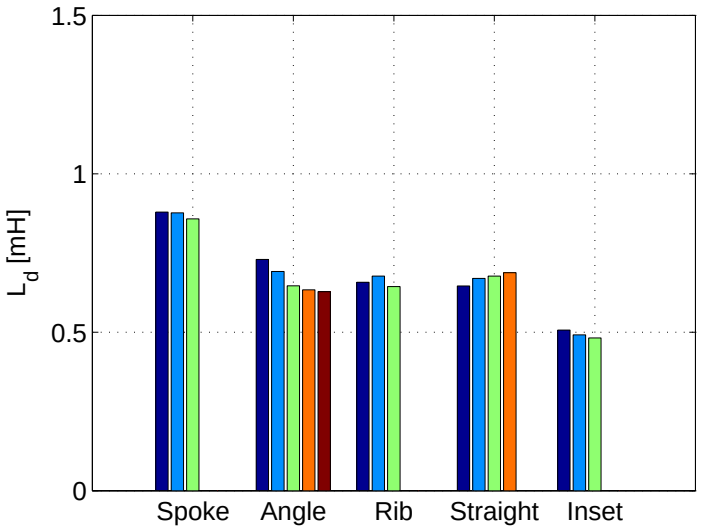

Figure 5.36: d-axis inductance variation for different designs.

Figure 5.37 shows the q-axis inductance variation for different sweeps and designs.

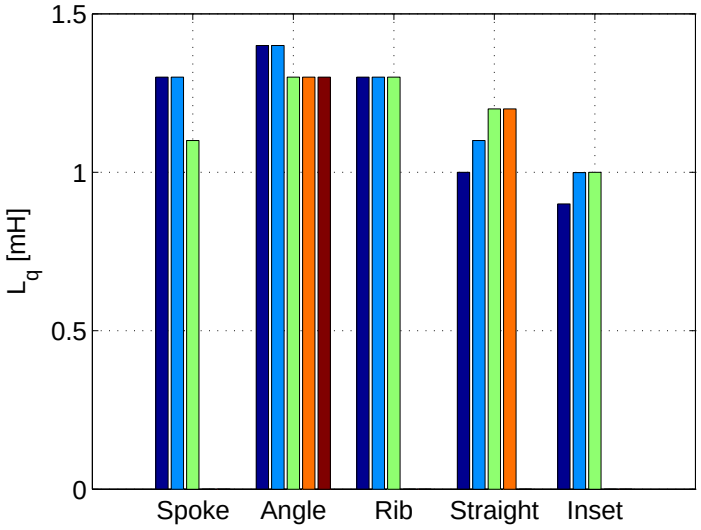

Figure 5.37: q-axis inductance variation for different designs.

It can be observed that the L_d and the L_q are varying with the geometry since the geometry affect the d-q flux linkages, as expected from (3.16) and

(3.17), as well as the simulations from the previous section.

Equation (3.21) shows the reluctance torque relation. It can be seen that the reluctance torque is a function of the difference between the d-q inductances. Figure 5.38 shows the absolute value of the difference between the d and q inductances for different designs.

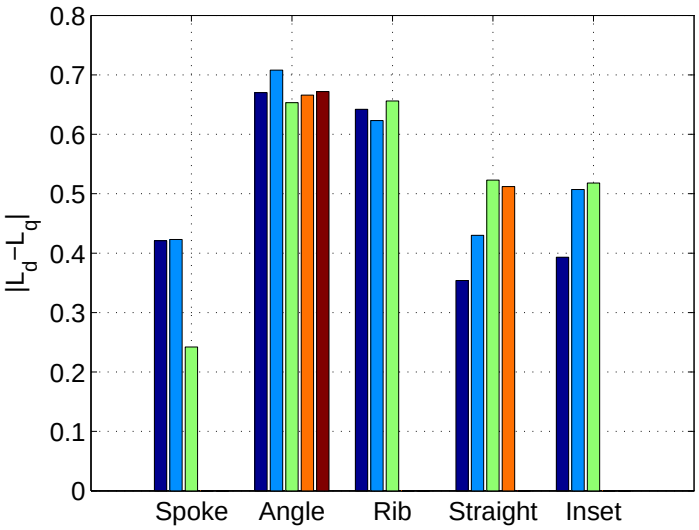

Figure 5.38: Inductance difference variation for different designs.

According to (3.21), the reluctance torque must behave similarly to the inductance difference as long as the operation point, hence the d-q currents remain the same. Figure 5.39 shows the reluctance torque variation for different designs.

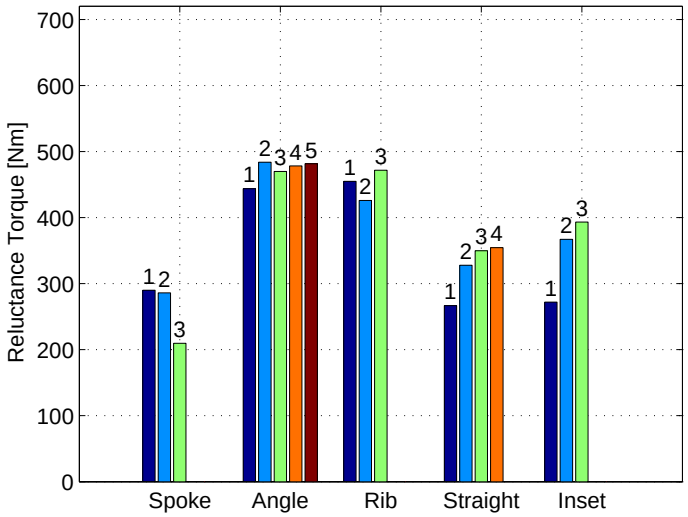

Figure 5.39: Reluctance torque variation for different designs.

As expected, the inductance difference and the reluctance torque variations are rather linked. The minor anomalies are caused by the slight differences in the current angle for different designs.

From (3.20), it is possible to acknowledge that the magnet torque of the generator is a function of the magnet flux. Figure 5.40 shows the variation of the magnet flux linkages for different designs.

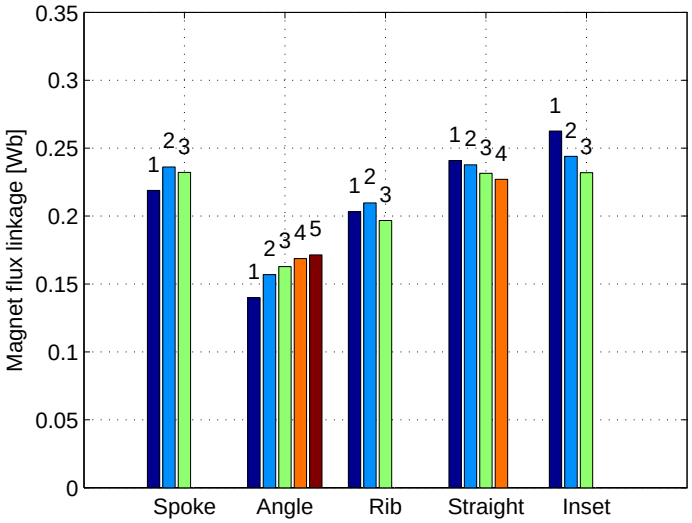

Figure 5.40: Magnet flux linkage variation for different designs.

The results are consistent with the simulations performed in the previous section. According to (3.20), the magnet torque is expected to vary in a similar fashion as the magnet flux linkage, as long as the current angle and magnitude are not changed. Figure 5.41 shows the variation of the magnet torque for different sweeps and designs.

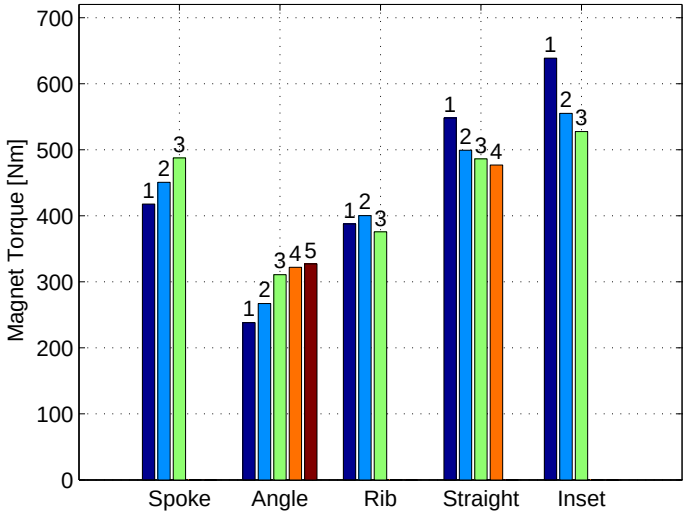

Figure 5.41: Magnet torque variation for different designs.

As explained above, the proportional behavior between Ψ_m and the magnet torque can be seen. The minor anomalies are caused by the slight differences in the q-axis current for different designs.

Equation (3.19) shows that the total torque is the summation of the magnet and reluctance torques. Figure 5.42 shows the total torque output from the different generator designs.

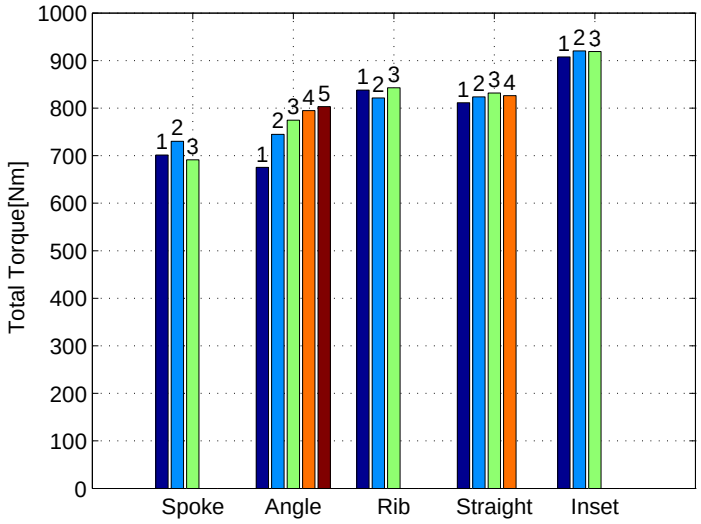

Figure 5.42: Optimal torque variation for different designs.

The total torque values are consistent with the simulations performed individually for different designs in the previous section. Table 5.1 shows the maximum magnet, reluctance and total torque values obtained from the different sweep and the design number at which it is obtained.

Table 5.1: Torque evaluation of each design.

Design	Magnet Torque	No	Reluctance Torque	No	Torque	No
Spoke	488	3	290	1	730	2
Inset	639	1	393	3	920	2
Angle	327	5	484	2	803	5
Rib	400	2	455	3	843	1
Straight	548	1	355	4	832	2

According to the results presented above, the second inset design is selected as the most suitable generator for the WEC, due to highest output torque, for the given current level.

5.4 System Integration of the Inset design

In this section, the inset design which was found to have the best performance replaces the initial electric generator as the selected generator for further investigations. The input to the generator is the mechanical torque supplied by the buoy. As stated previously, power curtailment level is 250 kW and that corresponds to a maximum torque of 800 Nm. Figure 5.43 shows the relation between the input torque and the input current of the generator.

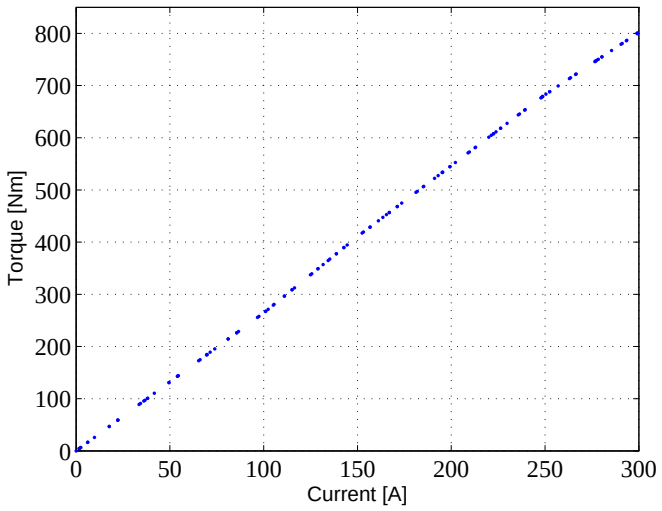

Figure 5.43: Average torque for different current levels for the inset design.

It can be seen that this generator reaches the rated torque at approximately 300 A, which is 50 A less compared to the initial case. Due to the lower torque level, lower losses are expected. Figure 5.44 shows the machine losses of the inset design.

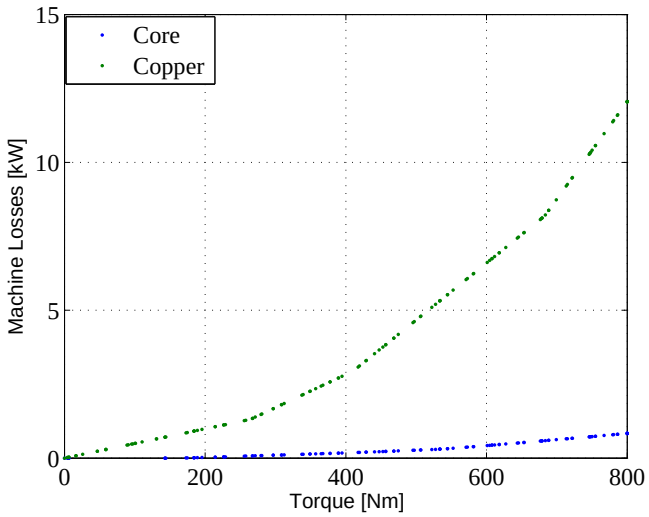

Figure 5.44: Machine losses of the inset design for different current levels.

It can be seen that the copper losses of the inset design are 12 kW and the core loss is approximately 0.85 kW. Figure 5.45 shows the converter losses of the inset design.

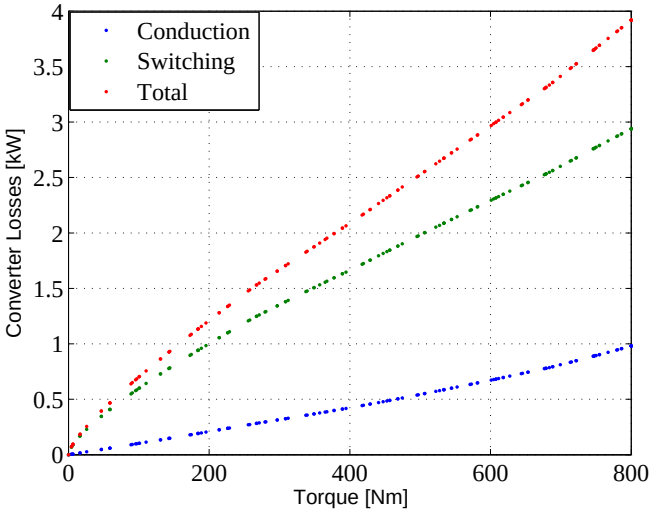

Figure 5.45: Converter losses of the inset design for different current levels.

It is seen that the conduction losses for this design is 0.98 kW and the switching losses end up at 2.94 kW. Compared with the results from the initial design, the improvement can be seen. The copper losses are decreased

by 22%, which shows the effect of the reduced current for the desired torque level. The efficiency of the inset design is depicted in Figure 5.46.

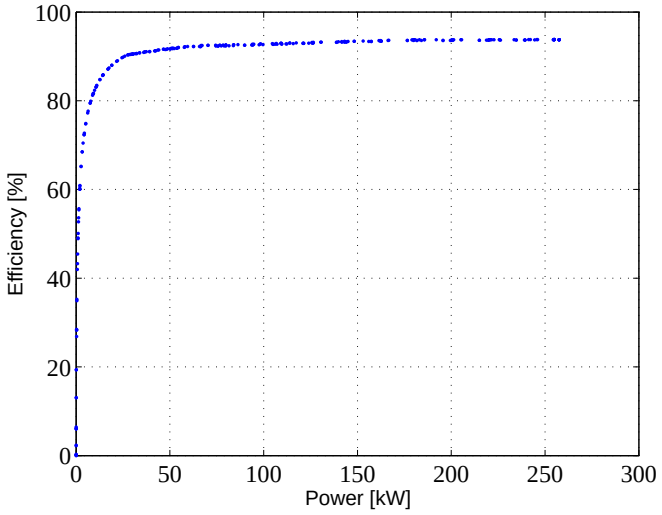

Figure 5.46: Drive system efficiency for the inset design.

The efficiency of the system for the rated torque is now approximately 95%. Compared with the initial design, the inset system has 1.35% higher efficiency.

5.5 Material Evaluation

In this section, the effects of different iron and magnet materials are investigated.

5.5.1 Evaluation of Different Iron Materials

In this section the electrical steel material used in constructing the stator and the rotor yokes of the electric generator is investigated. The material used in the initial design is $M19\_29G$ and will in the continuing be named steel 1 [35]. The second iron material is $M700\_50A$ [41] and it is a 0.5 mm thick lamination, named steel 2, which is a cheaper material. The third material is $M270\_35A$ [41], which is 0.35 mm thick electrical steel laminations and is named steel 3. Figure 5.47 shows the B-H curves for the used iron materials.

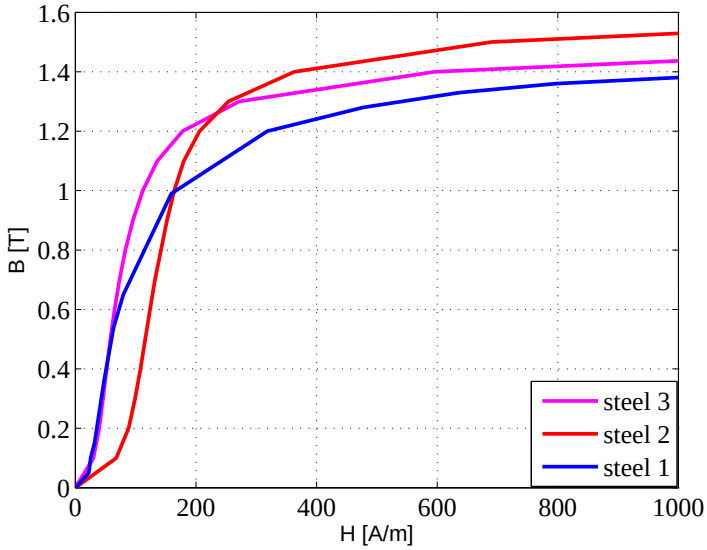

Figure 5.47: B-H curves for different iron materials.

It is seen that under 50 A/m field intensities, Steel 1 and Steel 3 have the same properties, while Steel 2 does not have a very good performance. However for values above 400 A/m Steel 2 can have a higher flux for a given magnetic field strength, followed by Steel 3 and then Steel 1.

Figure 5.48 shows the core loss for the rated electrical frequency for the iron materials.

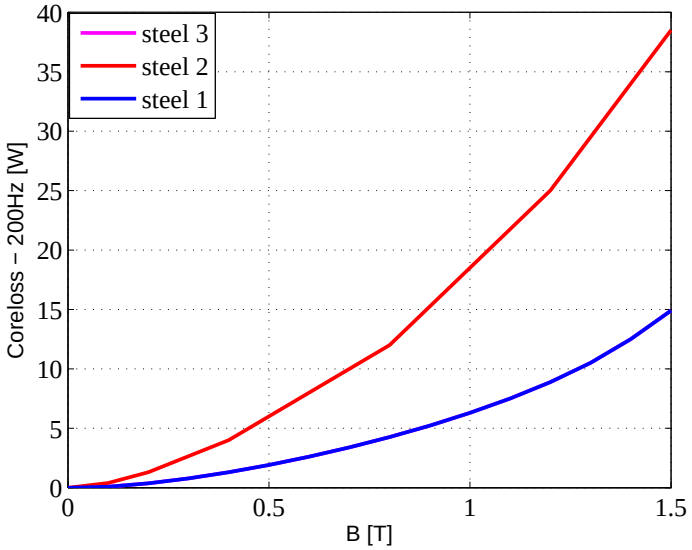

Figure 5.48: Coreloss for different iron materials for 200 Hz.

It can be seen that steel 2 has a very high core loss for the rated frequency, as expected. Steel 1 and steel 3 surprisingly have identical core loss relation.

5.5.2 Evaluation of the Permanent Magnet Material

The permanent magnet strengths are given by the value referred to as the magnetic coercivity [42]. The magnet material used in the initial design, N36Z_20 [35], is named Magnet 1 in this project. The coercivity of this magnet is $-920000A/m$. This material is replaced by Vac_745_HR, named Magnet 2, which has a magnetic coercivity of $-1073000A/m$ [43]. The coercivity values are given for 70^o magnet temperature.

5.5.3 Replacing the Initial Materials

In this section, the iron and the magnet materials of the generator are replaced by the materials mentioned previously.

Firstly, the iron material is replaced and each case is tested for the maximum input current. Table 5.2 shows the different torque outputs obtained at maximum current for different iron materials.

Table 5.2: Torque outputs for different electrical steel materials.

Design	Torque [Nm]
Steel 1	920
Steel 2	920
Steel 3	929

As it can be seen, the iron material has very little impact on the torque output. Using Steel 1 and Steel 2 provide the same torque output, however this is coincidental, since these two materials do not have similar properties. However Steel 1 has lower core loss for the rated frequency and Steel 2 has a higher flux density level for a given field strength. Steel 3 gives the highest torque output.

Table 5.3 shows output torque obtained for rated operation for different magnet materials.

Table 5.3: Torque outputs for different magnet materials.

Design	Torque [Nm]
Magnet 1	920
Magnet 2	1000

As expected, it can be noted that the magnet change improves the torque output greatly. It should be noted that the combination of Magnet 1 and Sheet 1 correspond to the initial generator design. It can be seen that using Magnet 2 and Steel 3 improves the machine performance, therefore, for the next case both the yoke and the magnet materials are replaced. Table 5.4 shows the torque output for the rated operation for changing both core and magnet materials.

Table 5.4: Torque outputs for different magnet and yoke materials.

Design	Torque [Nm]
Steel 1/Magnet 1	920
Steel 3/Magnet 2	1018

The idea to create a high efficiency design is thus achieved, as can be seen from the table above.

Table 5.5 shows the power losses for different cases while used as the generator for the investigated WEC for the maximum operating point.

Table 5.5: Power Losses for different cases used as a WEC generator

Design	Copper [W]	Core [W]	Conduction [W]	Switching [W]
Steel 1/Magnet 1	12050	836	980	2940
Steel 2/Magnet 1	12130	2841	985.8	2948
Steel 3/ Magnet 1	11910	896.5	975.2	2925
Steel 1/Magnet 2	9880	865.1	881.3	2010
Steel 3/Magnet 2	9653	899	868.8	1988

Here, it is seen that the improved machines do not require the maximum current, 350 A, as the initial V-shaped magnet design does, in order to reach the rated torque. Therefore, the improved cases have lower losses than the initial design. It can be seen that using Steel 2, which has higher core loss as shown in Figure 5.48, results in a high core loss value. The core loss obtained using Steel 2 is approximately 30% higher than those for Steel 1 and Steel 3. When the magnet changes are considered, it can be seen that the Steel 3/Magnet 2 design has the highest torque, therefore it requires the lowest current in order to achieve the rated torque. Due to that, it has the lowest copper and converter losses, since these are functions of the current. In addition, due to the B-H curve differences, using Steel 1 instead of Steel 3 results in lower core losses.

5.6 Energy Production and Loss Maps

In the previous chapter, the wave power and wave energy harnessed by a theoretical generator were shown. Here, the theoretical generator is replaced by the designs investigated. The selected designs are the initial generator, the inset design, the inset design with steel 2, the inset design with steel 3 and the inset design with the steel 3 and the magnet 2 material combination.

For the simulations, the buoy is represented as a torque source to the generator and the torque corresponding to $H-T$ combinations for the scatter diagram is calculated. The torque input is then used for selecting the d-q currents through the MTPA strategy. Thereon, the FEM calculations for each design is performed, using the corresponding d-q current inputs.

Figure 5.49 shows the machine losses for the initial design, simulated as described above.

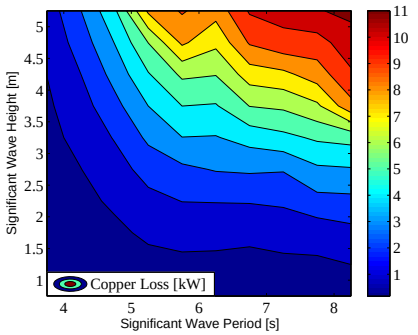

(a) Copper Loss.

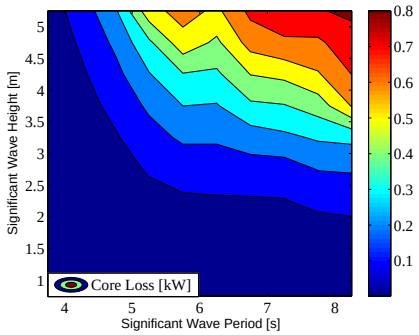

(b) Core Loss.

Figure 5.49: Machine Losses for the initial design.

Figure 5.50 shows the converter losses for the initial design.

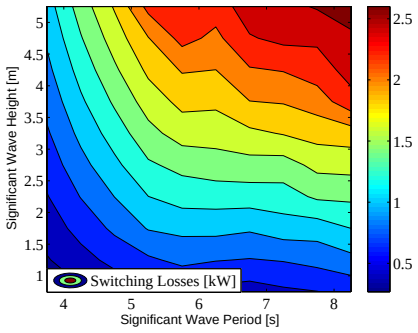

(a) Switching Losses.

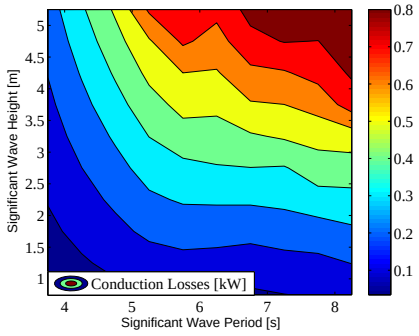

(b) Conduction Losses.

Figure 5.50: Converter Losses for the initial design.

These values agree with the two dimensional figures shown earlier. It is observed that for higher $H - T$ values, the losses increase, since the higher H-T values have higher wave power, which in return supplies a higher torque to the generator. Higher torque value would then demand a larger current, which results in larger losses.

Figure 5.51 shows the annual energy production and the annual energy loss obtained using the initial design.

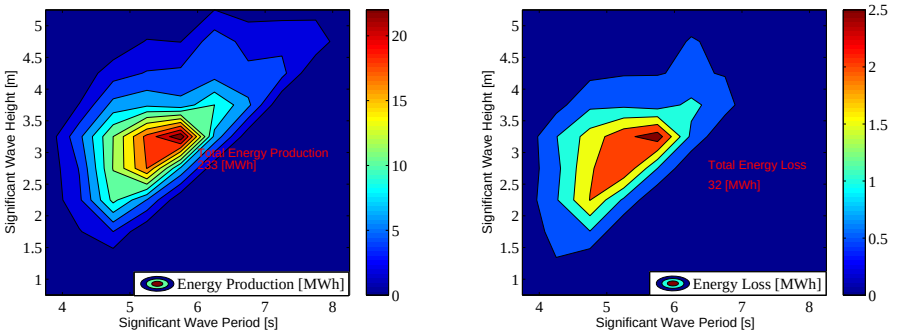

(a) Energy Production. (b) Energy Loss.

Figure 5.51: Produced and the lost energy for the initial design.

It can be seen that due to the probability distribution, the highest energy production and energy loss do not occur at the highest H-T combination. The same procedure is performed for each different design and similar graphs are obtained. Table 5.6 shows the annual energy productions and the annual energy losses of the selected designs.

Table 5.6: Annual Energy Production and Annual Energy Loss for different machine designs.

Design	Production [MWh]	Loss [MWh]
Initial	233	32
Inset	239	26
Steel 2/Magnet 1	237	28
Steel 3/Magnet 1	239	26
Steel1/Magnet 2	245	20
Steel 3/Magnet 2	246	19

Here it is seen that the initial design has the highest annual energy losses. It is followed by the steel 2 case, since it is a thick steel sheet which has a high loss density. Since steel 1 and steel 3 materials have similar properties, the annual energy production and the energy losses are the same. The design using the improved permanent magnet has the highest energy production and the lowest losses, as expected. In order to have a better understanding of the different topologies, the generator efficiencies are calculated. Table 5.7 shows the generator efficiencies for different generator selections for the rated operation point.

Table 5.7: The efficiency of different machines for the rated operation.

Design	Efficiency [%]
Initial	92.2
Inset	93.75
Steel 2/Magnet 1	93.76
Steel 3/Magnet 1	94.5
Steel1/Magnet 2	95.2
Steel 3/Magnet 2	95.3

As expected, the design with the improved magnets have the highest efficiency and the initial design has the lowest efficiency, however the Magnet 2 design has almost as good loss performance as the best one.

5.7 Economical Evaluation of the Different Generator Designs

In the previous sections the start up generator has been improved from the energy point of view, however this does not give us a complete picture about whether the improved designs are beneficial in average for the whole operation and if so to what degree. Accordingly, in this section, the life cycle cost analysis is done for the selected improved designs as well as the start up, in order to have a better understanding of the economic feasibility of the electric generation system used in the WEC.

First point of interest is the cost of the generator, which will be the investment cost of the electrical system. The investment cost consists of the cost of the materials used in constructing the machine and the manufacturing costs.

$$C_{investment} = m_{material}\Pi_{material} \tag{5.4}$$

where $m_{material}$ is the weight of the material used in the system and $\Pi_{material}$ is the corresponding price. Table 5.8 shows the material weights of the generators. The material weights are not different for different designs since the stator geometry is not changed and the magnet volume is kept constant.

Table 5.8: Weight of the different materials for the machine.

Material	Weight [kg]
Winding	3.57
Rotor	24.56
Stator	52.9
Magnets	3.6

The real wholesale prices of the materials are challenging to obtain, however in order to calculate the investment costs some crude assumptions are made. Table 5.9 shows the assumed prices for different materials used in this thesis.

Table 5.9: Assumed Material Prices.

Material	Price [SEK/kg]
Copper wire	1200
Sheet 1	30
Sheet 2	15
Sheet 3	35
NdFeB	800
Dysprosium	4300

Here the Magnet 1 material consists of 1% dysprosium, whereas Magnet 2 has 12% dysprosium.

The converter prices are not included since the same converter is used for each different design. Table 5.10 shows the investment costs of different generator designs.

Table 5.10: Investment costs of different electric generator designs.

Design	Investment Cost [kSEK]
Initial	14.8
Inset	14.8
Steel 2/Magnet 1	12.5
Steel 3/Magnet 1	15.6
Steel1/Magnet 2	17.7
Steel 3/Magnet 2	18.5

Here, the manufacturing cost is included as a coefficient and it is selected to be 2.

It can be seen that the improved magnet design has the highest investment cost as expected, since the permanent magnets are costly. The lowest cost design is the Steel 2/Magnet 1 design.

The second point of interest is how the generators behave during their operating time, which is investigated using the Net Present Value Method. In this thesis, instead of the cost of benefit, the cost of losses are used, therefore it will be called Net Present Value of Losses (NPVL) and is calculated as

$$NPVL = \frac{R_t}{(1+i)^t} \tag{5.5}$$

Here, R_t is the net cash flow, in this case the price of the energy loss per MWh, i is the interest rate and t is the life time [44]. Here, the life time is selected to be 20 years and the interest rate is 9%. The electricity price is assumed to be 400 SEK/MWh [45].

Table 5.11: Net Present Value of Losses for different electric generator designs.

Design	Net Present Value [kSEK]
Initial	117
Inset	95
Steel 2/Magnet 1	102
Steel 3/Magnet 1	95
Steel 1/Magnet 2	73
Steel 3/Magnet 2	69

It can be observed that the lowest NPVL is obtained while using the Steel 3/Magnet 2, since this design has the lowest energy loss. It is also seen that improving the initial design was highly motivated due to having the highest NPVL.

The Life Cycle Cost (LCC) of the system is then calculated by adding up the investment cost and the operational costs together [44]. The operational costs in this thesis are assumed to consist of the machine losses and the converter losses.

Table 5.12: Life Cycle Cost of using different electric generator designs.

Design	Life Cycle Cost [kSEK]
Initial	131.7
Inset	109.8
Steel 2/Magnet 1	114.8
Steel 3/Magnet 1	110.6
Steel 1/Magnet 2	90.8
Steel 3/Magnet 2	87.9

Figure 5.52 shows the investment costs, NPVLs and the LCCs of different designs.

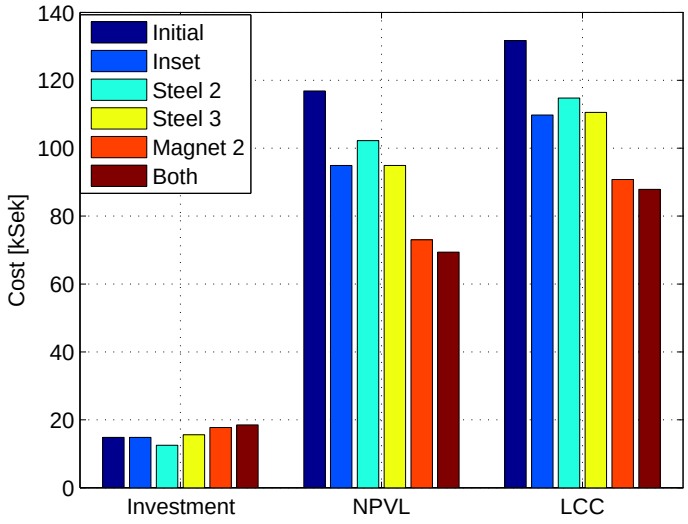

Figure 5.52: Economic Evaluation of different designs.

The economic evaluation shows that high losses of the initial generator design result in the highest LCC, even though the investment cost is relatively low. Similarly, the Steel 2/Magnet 1 design does not end up being the most economical solution, even though it has the lowest investment costs. The design where both the magnet and the core material is improved is the most economically beneficial design due to its low loss rate, even though the initial investment of the system is the most expensive. It was stated before that there is only 0.1% efficiency increase between the Steel1/Magnet 2 design and the Steel 3/ Magnet 2. Although the performance of the generator is

only slightly improved by replacing the core material, the LCC of the limited part of the system is improved approximately 4%.

Chapter 6

Conclusions and Future Work

6.1 Conclusions

In this thesis, different designs of PM generator rotors are investigated through FEM calculations and analytical simulations, in order to evaluate the power production through a WEC. First, the wave energy potential is investigated for the selected location and the possible harvestable wave energy is calculated using the passive power extraction method. An initial generator is designed based on the power requirement of the buoy and starting from this machine, adjustments regarding the rotor geometry and construction material are performed in order to increase the efficiency. The suitable designs are then investigated economically, using the net present value method.

The wave model is implemented using a state-space system and the buoy movement is simulated. High power carrying waves occur seldom and accordingly, the annual wave energy content is highest for a lower power level which is more probable to occur. Accordingly, power curtailment for the wave power production is fairly beneficial, since designing the system for the highest power level which occurs less than a few percent of the time increases the investment cost. This understanding motivates using power curtailment on the highest possible power and it is concluded that performing a 50% power curtailment corresponds to a mere 10% annual energy loss.

The electric machine performances were obtained through FEM calculations. By comparing the performance of different generator designs with different permanent magnet placements, it was observed that the inset permanent magnet design is more suitable than the two-piece magnet interior mounted design. For the identical materials and the same volume, the inset design has 1.3% higher efficiency than the interior magnet design, which corresponds to circa 15 kSEK improvement on the LCC for the same investment

cost.

Constructing the electric generator using materials with better performance increases the investment cost, however the investment cost is a small portion of the LCC of the machine. Here, between the least expensive (Sheet 2) and the more expensive (Magnet 2) designs, there is approximately 6 kSEK difference for the initial investment cost, however using a more efficient generator lowers the LCC of the wave energy system by more than 23 kSEK, due to its lower losses.

6.2 Future Work

The wave model in this project is selected to be regular, therefore the peak to average ratio of wave power was constant until the curtailment level is reached, then it increases slightly. Using irregular waves as input for WEC calculations would provide a more realistic picture of the wave power production. Another aspect to investigate later on is the active power extraction, where the point absorber movement is actively controlled in order to supply the highest torque to the generator.

This work mainly focuses on the permanent magnet generators, however due to the fluctuations in the rare earth magnet material prices, other machine types can be investigated for wave power operations, where the reluctance torque is greatly utilized. Some machine types which are valuable to consider are the ferrite magnet spoke rotor machine and the synchronous reluctance machine. The induction machine is also a worthy candidate for further studies. Moreover, investigating the torque ripple would be beneficial for a more thorough evaluation of the different generator performances. Adding a field weakening algorithm to the generator control would help further utilize the generator for different loads. A very valuable effort would be to include other parts of the WEC system, such as the gear-box and the rest of the WEC mechanical system in an optimization to determine the curtailment level.

Finally, constructing a small scale generator to test for the wave power production for comparing and evaluating the simulation results would be of interest.

References

[1] "Technology white paper on wave energy potential on the u.s. outer continental shelf," Minerals Management Service, May 2006. [Online]. Available: http://www.boem.gov/Wave-Energy-White-Paper-2006/

[2] M. Leijon, R. Waters, M. Rahm, O. Svensson, C. Bostrom, E. Stromstedt, J. Engstrom, S. Tyrberg, A. Savin, H. Gravrakmo, H. Bernhoff, J. Sundberg, J. Isberg, O. Agren, O. Danielsson, M. Eriksson, E. Lejerskog, B. Bolund, S. Gustafsson, and K. Thorburn, "Catch the wave to electricity," *Power and Energy Magazine, IEEE*, vol. 7, no. 1, pp. 50–54, January 2009.

[3] D. Kavanagh, A. Keane, and D. Flynn, "Capacity value of wave power," *Power Systems, IEEE Transactions on*, vol. 28, no. 1, pp. 412–420, Feb 2013.

[4] Wikipedia, "List of wave power stations — wikipedia, the free encyclopedia," May 2015, [Online; accessed 17-May-2015]. [Online]. Available: http://en.wikipedia.org/w/index.php?title=List_of_wave_power_stations&oldid=653451395

[5] A. Bozzetto and E. Tedeschi, "Wave power extraction with constrained power take-off: Single capture vs. double capture point absorbers," in *Ecological Vehicles and Renewable Energies (EVER), 2014 Ninth International Conference on*, March 2014, pp. 1–7.

[6] M. Leijon, O. Danielsson, M. Eriksson, K. Thorburn, H. Bernhoff, J. Isberg, J. Sundberg, I. Ivanova, E. Sjostedt, O. Agren, K. Karlsson, and A. Wolfbrandt, "An electrical approach to wave energy conversion."

[7] S. Tyrberg, O. Svensson, V. Kurupath, J. Engstrom, E. Stromstedt, and M. Leijon, "Wave buoy and translator motions; on-site measurements and simulations," *Oceanic Engineering, IEEE Journal of*, vol. 36, no. 3, pp. 377–385, July 2011.

[8] K. Yuen, K. Thomas, M. Grabbe, P. Deglaire, M. Bouquerel, D. Osterberg, and M. Leijon, "Matching a permanent magnet synchronous generator to a fixed pitch vertical axis turbine for marine current energy conversion," *Oceanic Engineering, IEEE Journal of*, vol. 34, no. 1, pp. 24–31, Jan 2009.

[9] I. Ivanova, O. Agren, H. Bernhoff, and M. Leijon, "Simulation of cogging in a 100 kw permanent magnet octagonal linear generator for ocean wave conversion," in *Underwater Technology, 2004. UT '04. 2004 International Symposium on*, April 2004, pp. 345–348.

[10] S. Tyrberg, R. Waters, and M. Leijon, "Wave power absorption as a function of water level and wave height: Theory and experiment," *Oceanic Engineering, IEEE Journal of*, vol. 35, no. 3, pp. 558–564, July 2010.

[11] S. Bozzi, A. Miquel, F. Scarpa, A. Antonini, R. Archetti, G. Passoni, and G. Gruosso, "Wave energy production in italian offshore: Preliminary design of a point absorber with tubular linear generator," in *Clean Electrical Power (ICCEP), 2013 International Conference on*, June 2013, pp. 203–208.

[12] A. Naikodi and G. Sridhara Rao, "Efficient operation of ac voltage controller fed induction machine for wave power generation," in *Power Electronics, Drives and Energy Systems for Industrial Growth, 1996., Proceedings of the 1996 International Conference on*, vol. 1, Jan 1996, pp. 265–270 vol.1.

[13] E. Enferad and D. Nazarpour, "Implementing double fed induction generator for converting ocean wave power to electrical," in *Power Electronics, Drive Systems and Technologies Conference (PEDSTC), 2013 4th*, Feb 2013, pp. 448–453.

[14] E. Enferad, M. Farsadi, and S. Enferad, "Application of pmsm for electric generation from ocean waves by epew," in *Electrical and Electronics Engineering (ELECO), 2011 7th International Conference on*, Dec 2011, pp. I–258–I–262.

[15] M. Toulabi, J. Salmon, and A. Knight, "Design and performance assesment for the v shaped magnet ipm synchronous motor," in *IEMDC 2015, Coeur dAlene, Idaho, USA*, May 2015, pp. 214–219.

[16] M. Chowdhury, M. Islam, A. Gebregergis, and T. Sebastian, "Robust design optimization of permanent magnet synchronous machine utilizing

genetic and taguchi's algorithm," in *Energy Conversion Congress and Exposition (ECCE), 2013 IEEE*, Sept 2013, pp. 5006–5012.

[17] R. Liu, X. Sun, J. Gong, and S. Guo, "Comparison of different arrangement of magnets for the purpose of reducing magnet usage in designing an ipm motor for electric vehicles," in *Transportation Electrification Asia-Pacific (ITEC Asia-Pacific), 2014 IEEE Conference and Expo*, Aug 2014, pp. 1–5.

[18] K. Khan, M. Leksell, and O. Wallmark, "Design aspects on magnet placement in permanent-magnet assisted synchronous reluctance machines," in *Power Electronics, Machines and Drives (PEMD 2010), 5th IET International Conference on*, April 2010, pp. 1–5.

[19] P. Roshanfekr, T. Thiringer, M. Alatalo, and S. Lundmark, "Performance of two 5 mw permanent magnet wind turbine generators using surface mounted and interior mounted magnets," in *Electrical Machines (ICEM), 2012 XXth International Conference on*, Sept 2012, pp. 1041–1047.

[20] J. Falnes, *Ocean Waves and Oscillating Systems: Linear Interactions Including Wave-Energy Extraction*. Cambridge University Press, 2002. [Online]. Available: https://books.google.se/books?id=bl1FyQjCklgC

[21] D. C. Hong and K. Y. Hong, "Performance prediction of an owc wave power plant," in *OCEANS, 2012 - Yeosu*, May 2012, pp. 1–5.

[22] E. Tedeschi and M. Molinas, "Tunable control strategy for wave energy converters with limited power takeoff rating," *Industrial Electronics, IEEE Transactions on*, vol. 59, no. 10, pp. 3838–3846, Oct 2012.

[23] A. Babarit, B. Borgarino, P. Ferrant, and A. Clément, "Assessment of the influence of the distance between two wave energy converters on energy production," *Renewable Power Generation, IET*, vol. 4, no. 6, pp. 592–601, November 2010.

[24] L. Bergdahl, "Wave-induced loads and ship motions," Chalmers University of Technology, Gothenburg, Sweden, 2010.

[25] M. Johansson, *Transient Motions of Large Floating Structures*. Institutionen för vattenbyggnad, Chalmers tekniska högskola, 1986.

[26] R. Rajput, *A Textbook of Electrical Engineering*. Laxmi Publications Pvt Limited, 2004. [Online]. Available: https://books.google.se/books?id=k22bKyWqWD0C

[27] L. Harnefors, "Control of variable speed drives," Mälardalen University, Västerås Sweden, 2002.

[28] J. Härsjö, *Modeling of PMSM Full Power Converter Wind Turbine with Turn-To-Turn Fault.* Göteborg: Institutionen för energi och miljö, Chalmers tekniska högskola, 2014, 120.

[29] J. Hendershot and M. T.J.E., *Design of Brushless Permanent-Magnet Motors.* Magna Physics Publications - Oxford University Press, 2010.

[30] N. Mohan, T. M. Undeland, and W. P. Robbins, *Power Electronics. Converters, Applications and Design*, 3rd ed. John Wiley and Sons, Inc, 2003.

[31] Infineon, "Datasheet, fz600r17ke4," unpublished. [Online]. Available: http://www.infineon.com/dgdl/Infineon-FZ600R17KE4-DS-v02_02-en_de.pdf?folderId=db3a304412b407950112b4095b0601e3&fileId=db3a3043293a15c401294a1c37557de9

[32] Semikron, "Determining switching losses of igbt modules," unpublished. [Online]. Available: http://www.semikron.com/dl/service-support/downloads/download/semikron-application-note-an-1403-switchinglosses-en

[33] O. Josefsson, *Investigation of a Multilevel Inverter for Electric Vehicle Applications*, ser. Doktorsavhandlingar vid Chalmers tekniska högskola. Ny serie, no:. Göteborg: Institutionen för energi och miljö, Elteknik, Chalmers tekniska högskola, 2015, 146.

[34] J. Hsu, A. C.W., and C. C.L., "Report on toyota/prius motor design and manufacturing assesment," 2004, unpublished. [Online]. Available: http://myprius.co.za/120761.pdf

[35] Ansys, "Ansys maxwell 2d field simulator v14 user's guide," unpublished.

[36] G. Dajaku and D. Gerling, "Air-gap flux density characteristics of salient pole synchronous permanent-magnet machines," *Magnetics, IEEE Transactions on*, vol. 48, no. 7, pp. 2196–2204, July 2012.

[37] E. Grunditz, *BEV Powertrain Component Sizing With Respect to Performance, Energy Consumption and Driving Patterns.* Göteborg: Institutionen för energi och miljö, Elteknik, Chalmers tekniska högskola,, 2014, 171.

[38] S. T. Lundmark, "Radial and transverse flux ipm core and magnet loss in fem 2d and 3d," Chalmers University of Technology, Gotherburg Sweden, Technical Report 2015:2, 2015.

[39] C. Zhao, Y. Wang, and Y. Yan, "Fem analysis of auxiliary poles of ipm synchronous machine with "flux concentration function"," in *Power Electronics and Drives Systems, 2005. PEDS 2005. International Conference on*, vol. 2, Nov 2005, pp. 1003–1008.

[40] C. Zhao, D. Zhu, and Y. Yan, "The optimization of auxiliary poles of ipm synchronous machine," in *Electrical Machines and Systems, 2005. ICEMS 2005. Proceedings of the Eighth International Conference on*, vol. 1, Sept 2005, pp. 344–349 Vol. 1.

[41] Surahama, "Non oriented electrical steel, typical data," unpublished. [Online]. Available: http://www.sura.se/Sura/hp_products.nsf/vOpendocument/03A8B2433FAE16C4C1256AA8002280E6/$FILE/datasheets.pdf?OpenElement

[42] C. Chen, *Magnetism and Metallurgy of Soft Magnetic Materials*, ser. Dover Books on Physics Series. Dover Publications, 1977, pp. 126-128. [Online]. Available: https://books.google.se/books?id=ufGdyu24X2EC

[43] Vacuumschmelze, "Datasheet, vacodym 745 hr," unpublished. [Online]. Available: http://www.vacuumschmelze.com/index.php?id=233

[44] O. Žižlavský, "Net present value approach: Method for economic assessment of innovation projects," *Procedia - Social and Behavioral Sciences*, vol. 156, no. 0, pp. 506 – 512, 2014, 19th International Scientific Conference, Economics and Management 2014 (ICEM-2014). [Online]. Available: http://www.sciencedirect.com/science/article/pii/S1877042814060509

[45] "NordPoolSpot." [Online]. Available: http://nordpoolspot.com

Appendix A

Machine Geometry Data

Table A.1: Stator Geometry for FEM simulation, type 0 for core

Stator outer diameter	269 mm
Stator inner diameter	161.9 mm
Number of slots	48
Slot Type	2
Slot opening height	1.03 mm
Slot closed bridge height	0
Slot wedge height	0
Slot body height	29.5 mm
Slot opening width	1.93 mm
Slot wedge maximum width	5 mm
Slot body bottom width	8 mm
slot body bottom fillet	5 mm

Table A.2: Rotor Geometry for initial design, type 0 for core and type 1 for magnet

Rotor outer diameter	160.4 mm
Rotor inner diameter	90.64 mm
Number of Poles	8
Pole Type	3
Limited diameter of PM ducts	157.4 mm
Bottom Width	3
Distance from duct bottom to shaft surface	7.28
Duct thickness	4.7 mm
Rib width	14 mm
Rib height	3 mm
Minimum distance between side magnets	4.5 mm
Magnet thickness	6.48 mm
Total width of all magnet per pole	32 mm

Table A.3: Rotor Geometry for inset design, type 0 for core and type 1 for magnet

Rotor outer diameter	160.4 mm
Rotor inner diameter	85 mm
Number of Poles	8
Pole Type	5
Limited diameter of PM ducts	158 mm
Bottom Width	0
Distance from duct bottom to shaft surface	28.28 mm
Duct thickness	6 mm
Rib width	10 mm
Rib height	4 mm
Minimum distance between side magnets	0.1 mm
Magnet thickness	7 mm
Total width of all magnet per pole	33.4 mm